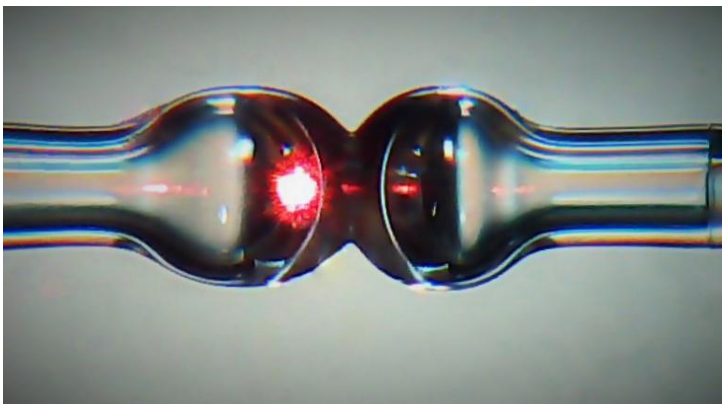

Optical Sensors Based on Fabry-Perot Interferometry

Catarina Silva Monteiro
Integrated Masters in Engineering Physics

Physics and Astronomy Department
2016

Supervisor
Orlando José Reis Frazão, Invited Assistant Professor, Faculty of Sciences of the University of Porto

U.PORTO

FACULDADE DE CIÊNCIAS
UNIVERSIDADE DO PORTO

Todas as correções determinadas pelo júri, e só essas, foram efetuadas.

O Presidente do Júri,

Porto, _____/_____/_____

Acknowledgements

To my supervisor, Dr. Orlando Frazão, who introduced me to an investigation environment and kept challenging me to work and search further. The knowledge and patience brought where essential for the development of this work.

To Dr. Marta Ferreira, for easing my entrance in the investigation environment. All the help given and knowledge were essential for my growth as an investigator.

To all my colleagues from INESC-TEC, in special those from the Centre of Applied Photonics for sharing all the knowledge and new ideas. António Rodrigues, Miguel Ferreira, Regina Magalhães, Tiago Martins and André Gomes, thank you!

I would like to acknowledge the ERDF – European Regional Development Fund through the Operational Programme for Competitiveness and Internationalization - COMPETE 2020 Programme within the project «POCI-01-0145-FEDER-006961», and by National Funds through the FCT – Fundação para a Ciência e a Tecnologia (Portuguese Foundation for Science and Technology) as part of project UID/EEA/50014/2013 which funded a vital part of my work for the thesis.

To INESC-TEC and the department of physics and astronomy of the Science Faculty of Porto University for the technical support and for the given opportunities to all the students to pursue their formation and grow as an investigator and as a scientist.

I would like to acknowledge professor Maria Teresa Restivo and professor Paulo Abreu for the cooperation between the two institutions that allowed the fabrication of embedded optical sensors. I would like to acknowledge Bruno Santos that easy the imprinting process.

To António Vaz Rodrigues, who helped me through the long hours in the lab and solving all the seemingly impossible problems with ingenious ideas. To Miguel Ferreira, Vanessa Boucinha and Ana Gomes for all the patience and help given through all the course of the work. To Filipa Barbosa, for helping me see the big picture when I failed to see. Thank you so much!

To my parents, for always believing that I could achieve everything that I set out to do and for helping me to do so. To my sister, who always made me believe that I could do everything in life. Thank you all so much.

Resumo

Os sensores em fibra ótica oferecem múltiplas vantagens em relação a dispositivos de deteção tradicionais. O vasto desenvolvimento de sensores em fibra ocorreu após o desenvolvimento do laser e o aperfeiçoamento das características das fibras óticas, em particular a diminuição de perdas por atenuação. Desde o final dos anos 60, os sensores foram objeto de investigação e desenvolvimento e apresentam hoje múltiplas aplicações.

A fibra ótica oferece um meio versátil para a produção sensores. As estruturas interferométricas são uma solução na fabricação de sensores com alta sensibilidade. Em particular, a interferometria de Fabry-Perot destaca-se pela facilidade de fabricação apresentando já aplicações na deteção e monitorização de vários parâmetros físicos, químicos e biológicos. O trabalho descrito nesta dissertação de mestrado está focado no desenvolvimento de novos sensores em fibra ótica baseados em interferometria de baixa finesse de Fabry-Perot, com recurso a tubos de sílica ocos.

A fabricação de um sensor de curvatura com baixa sensibilidade à temperatura foi objeto de estudo. O sensor desenvolvido é facilmente reprodutível uma vez que o processo de fabricação não depende de métodos dispendiosos.

A possibilidade de usar microbolhas de sílica, ou microesferas ocas, para a formação da cavidade de Fabry-Perot foi também abordada nesta dissertação. O sensor é fabricado usando apenas *fusion splicing*, que permite a produção de um sensor a baixo custo facilmente reprodutível. Sensores estruturados no extremo da fibra com uma microbolha de sílica foram usados para a deteção de carga lateral e temperatura. O alinhamento de duas microbolhas permite criar um sensor de deformação de alta sensibilidade.

A impressão 3D é outro dos temas abordados nesta dissertação. Recorrendo a uma impressora 3D, foi desenvolvida uma estrutura de encapsulamento para sensores com microbolhas. O encapsulamento das cabeças sensoras permitiu aumentar a gama dinâmica de funcionamento, evitando a danificação da cabeça sensora na aplicação de carga lateral.

O trabalho desenvolvido nesta dissertação de mestrado pode ser mais aprofundado e aprimorado, em particular os sensores embebidos na estrutura 3D impressa. O uso de diferentes materiais de encapsulamento poderá permitir a criação

de um sensor com maior sensibilidade aos parâmetros externos. Diferentes geometrias ou dimensões da estrutura poderão ainda permitir uma melhoria significativa dos resultados.

Palavras-chave: sensores em fibra ótica, interferometria de Fabry-Perot, impressão 3D, microesferas.

Abstract

Optical fiber sensors provide multiple advantages over traditional detection devices. The vast development of fiber sensors happened after the advances in the laser technology and the improvement of the optical fiber characteristics, in particular the reduction on the losses due to attenuation. Since the late 1960's, sensors were a matter of research and development and now present multiple applications.

Optical fiber offer a versatile mean for sensor production. Interferometric structures are presented as a solution for high sensibility sensors. Fabry-Perot interferometry, specifically, stands out for their easy fabrication processes and have many applications in detection and monitoring of several physical, chemical and biological parameters. The work described over this masters' thesis is focused on the development of newly optical sensors based on low finesse Fabry-Perot interferometry, resorting to hollow silica tubes.

The fabrication of a curvature sensor with low temperature sensitivity was a matter of study. The proposed sensor is easily reproducible since the fabrication process does not rely on expensive and time consuming methods.

The possibility of using microbubbles of silica, or hollow microspheres, to the formation of the Fabry-Perot cavity was, likewise, approached in this dissertation. The sensor was fabricated using only fusion splicing techniques, which allowed the production of a low cost sensor easily reproducible. Silica microbubble fiber tip sensors were used for the detection of lateral loading and temperature. The coupling of two microbubbles allowed the fabrication of a highly sensitive strain sensor.

Three dimensional printing is other addressed theme in the dissertation. Resorting to a 3D printer, an embedding structure for microbubble fiber tip sensors was fabricated. The encasing of the sensing heads allowed the increase of the dynamic range of operation, avoiding damage caused by the application of lateral loading on the sensing head.

The work undertaken in this masters' dissertation can be further explored and improved, in particular the 3D embedded sensors. The use of different materials in the encasing of the sensors could improve the sensors sensitivity to external parameters.

Different geometries or dimensions of the structure can, also, allow a significant improvement on the results.

Keywords: optical fiber sensors, Fabry-Perot interferometry, 3D printing, microspheres.

Table of Contents

List of Figures

List of Tables

List of Acronyms

AC	Alternating Current
DC	Direct Current
DMF	Dimethyl formamid
F	Coefficient of Finesse
FP	Fabry-Perot
HCPCF	Hollow Core Polymeric Fiber
MMF	Multimode Fiber
OPD	Optical path difference
OSA	Optical spectrum analyser
PCF	Photonic Crystal Fiber
PLA	Polylactic Acid
POFBG	Polymer optical fiber Bragg gratting
R	Reflectance
RI	Refractive Index
SMF	Single mode fiber
T	Transmittance

Chapter 1

Introduction

1.1 Motivation

Precise and non-invasive measurements was always the main motivation for the development of new sensing techniques. Optical sensors present a great solution to overcome other, more traditional, techniques. Optical sensors also present a versatile solution for sensing purposes due to the wide range of independent parameters that can be accessed. This parameters may include intensity, phase, polarization and wavelength spectrum that can be sensitive to numerous of external factors [1].

Optical sensing was revolutionized, in the 1960's, by the implement of optical fiber. This was only possible after the development of a coherent light source, the laser. The use of optical fiber allowed not only the development of electromagnetic interference immune sensors but also permits remote access measurements. The employment of optical fiber in sensing techniques presents multiple advantages over conventional sensors since optical fiber grants a higher accuracy while having smaller dimensions, high flexibility and small propagation losses [2]. Some more specific characteristics of optical fiber allows its use in biomedical applications [3] – optical fiber is biocompatible, inert, has low thermal conductivity, and presents a good adhesion to biological tissues.

One of the key parameters for sensing purposes is pressure. Pressure sensing relying on optical fiber is not a recent topic – it has been a matter of research since late 1970's [4]. However, sensing mechanisms for pressure using optical fiber are still not quite well developed and are still not seen as good replacements over more conventional solutions. Even though optical fiber sensors can be developed with low cost processes, their performance and endurance on harsh environments are still lacking improvements.

Fabry-Perot interferometry constitutes one of the main interferometer configurations applied on optical fiber. The resource to Fabry-Perot interferometry for pressure sensing is still a matter of research in the present time. Fabry-Perot based

sensors can be easily developed and implemented, with cost effectiveness. This makes Fabry-Perot interferometry an appealing solution in optical fiber sensing mechanisms. This constitutes the main theme explored over this dissertation.

1.2 Aim and Objectives

The aim of this dissertation is to develop new optical fiber sensors based on Fabry-Perot interferometry applied in sensing of physical parameter as curvature, strain and pressure.

The following objectives were established:

- Development of new designs of optical fiber sensors for strain, curvature and other physical parameters enhancing the sensor accuracy, resorting to fiber Fabry-Perot sensors based on hollow core silica fiber.
- Development of Fabry-Perot sensors with new designs, in order to create a highly sensitive sensor to pressure.
- Development of 3D structures for sensor packaging, utilizing to a 3D printer.
- Explore Fabry-Perot pressure sensors embedded using a 3D printer.

1.3 Structure of the dissertation

This thesis dissertation is divided into seven chapters, of which five are relative to experimental work developed in the dissertation framework.

In Chapter 1, the motivation of the dissertation is presented, followed by the objectives and the list of publications that resulted from this work.

Chapter 2 contains the state of the art of fiber Sensors based on Fabry-Perot interferometry. A brief introduction of sensor technology is given, proceeded by physical explanation of the Fabry-Perot interferometer operation. An historical overview of Fabry-Perot based sensors is presented, where the main publications on the subject are explored.

In Chapter 3 a curvature sensor based on Fabry-Perot interferometry is proposed. The sensor structure is composed by a hollow core fiber cavity exposed to

small curvatures radius. Low thermal sensitivity, the sensor is suitable to harsh environments applications.

Chapter 4 is focused on a lateral loading sensor, with a new hollow microsphere tip sensor. The sensor, fabricated only by fusion splicing techniques, provides an all-silica solution for lateral loading measurements with low temperature sensitivity.

Over Chapter 5, a sensor based on two coupled hollow microspheres is presented. The developed sensors were tested for strain, curvature and temperature, providing high strain sensitivity.

In Chapter 6, a tip sensor based on a hollow microsphere cavity embedded in a 3D printed structure is presented. The sensor, developed with the previous addressed fabrication steps, was embedded in a polymeric structure and tested for lateral loading and temperature. The packaging of the Fabry-Perot sensor provided grounds to enlarge the dynamic range of measurements.

Chapter 7 features the concluding remarks of the work, summarizing its main achievements. Future work possibilities is the other topic presented.

1.4 Outputs

Scientific Journals

C. S. Monteiro, M. S. Ferreira, S. O. Silva, J. Kobelke, K. Schuster, J. Bierlich, and O. Frazão, “Fiber Fabry-Perot interferometer for curvature sensing,” *Photonic Sensors*, pp. 1–6, 2016, DOI: 10.1007/s13320-016-0333-9.

Communications in National/International Conferences

C. S. Monteiro, and O. Frazão, *“Optical fiber pressor sensor based microsphere structure embedded polymer material,”* SEONs 2016 – XIII Symposium on Enabling Optical Networks and Sensors, Covilhã, Portugal, 2016. **(Oral Presentation)**

C. S. Monteiro, M. S. Ferreira, J. Kobelke, K. Schuster, J. Bierlich, and O. Frazão, *“Curvature sensors based on a Fabry-Perot interferometer,”* EWOFS'2016 – Sixth European Workshop on Optical Fibre Sensors, Ireland, 2016, DOI: 10.1117/12.2235215.

Chapter 2

State-of-the-art of Fiber Sensors Based on Fabry-Perot Interferometry

The technology behind optical fiber sensors is present for several decades and it has multiple advantages over conventional electric sensing mechanisms. Optical fiber is immune to electromagnetic interference, has small dimensions and is lightweight, presents high accuracy and resolution, is capable of remote operation and is suited to be applied in harsh environments. Optical fiber sensors based on an interferometric configuration are the topic of this dissertation. Mach-Zehnder [5], Michelson [6], Sagnac [7] and the low finesse Fabry-Perot (FP) [8] are the most explored and simple interferometric configurations in optical fiber. The last mentioned will be the configuration studied over this dissertation.

Optical fiber configurations based on FP interferometry are very versatile and constitute a very compelling solution for sensing applications. FP optical sensors can be designed to be intensity or phase modulated, either intrinsic or extrinsic, and present high sensitivity to both physical and chemical parameters. Optical sensors based on low finesse FP interferometer are widely explored in the literature and have found applications in strain [9, 10], temperature [11], pressure [12–14] and magnetic fields [15, 16] measurements, among other important physical or chemical parameters.

In this chapter the basic working principles of fiber FP interferometer are presented, followed by an historical overview over FP interferometric configurations applied in optical fiber sensors.

2.1 Fabry-Perot fiber interferometer

Interferometric optical fiber sensors rely on the principle of optical interference for the measurement of physical or chemical properties. These sensors can exhibit great sensitivity, a wide dynamic range, multiplexing capacity and low losses, making them a great solution for sensing purposes.

In an interferometric configuration the incident light is divided into multiple beams. One or more beams will experience a change in the optical path due to physical or chemical changes in the surrounding environment. This will translate on a phase difference between these beams and a reference beam.

The low finesse FP interferometric configuration can be approximated as a two beam interferometer. In the present case, the incident light is divided in two different beams. One of the beams interacts with the measurand – the physical or chemical parameter intended to be measured – and the other will serve as a reference. In Fig. 2.1, an example of a fiber FP cavity is presented.

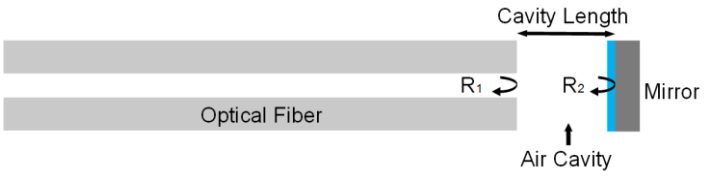

Fig. 2.1 Schematic of a fiber FP interferometer.

The intensity of the light that is reflected back to the optical fiber is the result of the interference of the two beams – the reference and the beam that interacts with the measurand. The total reflected light intensity is given by:

$$I_r(\lambda) = I_1(\lambda) + I_2(\lambda) + \sqrt{I_1(\lambda)\, I_2(\lambda)}\, cos(\phi) \tag{2.1}$$

Where I_1 and I_2 are the intensity of beam 1 and beam 2 respectively, and ϕ is the phase difference between the beams, due to optical path difference. The phase difference, ϕ, is given by:

$$\phi = 2\, k\, n_{eff} L\, cos\,\theta + \varphi \tag{2.2}$$

Where k is the wave vector, given by $\frac{2\pi}{\lambda}$, with λ being the wavelength; n_{eff} the effective refractive index of the cavity material and L the cavity length. The angle θ is the angle between the plane of incidence and the light direction. The φ indicates a phase shift introduced by the material, when the light goes through different media. When the interferometric configuration is implemented in optical fiber, the angle θ is small and $cos\,\theta$ can be approximated to 1, and φ can be neglected. The quantity

$2n_{eff}L$ is often known as optical path difference (OPD). The previous equation can be simplified, for a fiber FP interferometer, as:

$$\phi = 2\,k\,n_{eff}L \tag{2.3}$$

Considering that both surfaces have the same *reflectivity*, r, the total reflected intensity is given by:

$$I_r = I_i \frac{2R(1-cos\,\phi)}{1+R^2-2R\,cos\,\phi} \tag{2.4}$$

Where R is the reflectance is given by rr^*. The previous equation can be simplified by introducing a parameter, the coefficient of finesse, *F,* given by:

$$F = \left(\frac{2r}{1-r^2}\right)^2 = \frac{4R}{(1-R)^2} \tag{2.5}$$

The total transmitted intensity can be derived from the relation $T + R = 1$, where T is the transmittance. From that, is achieved:

$$\frac{I_t}{I_i} = \frac{T^2}{1+R^2-2R\,cos\,\phi} = \frac{1}{1+Fsin^2(\phi/2)} \tag{2.6}$$

This relation is also known as the Airy function ($A(\delta)$). The reflected and transmitted spectrum can be simulated by a simple Python code. In Fig. 2.2 and Fig. 2.3, the low finesse spectrum is presented, for different values of *F*, with ϕ ranging from -3π to 3π with a $\pi/20$ step.

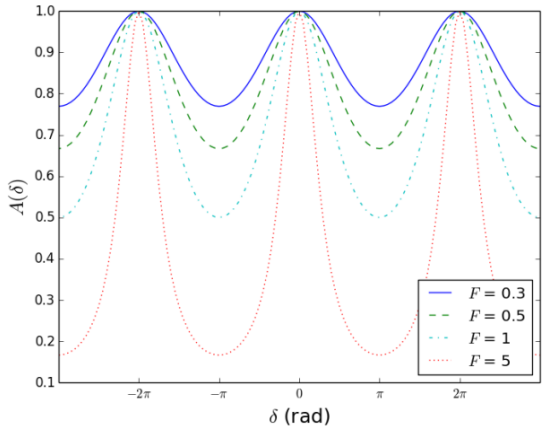

Fig. 2.2 Transmitted spectrum of a low finesse FP interferometer, for different coefficients of finesse (F=0.3, 0.5, 1, 5).

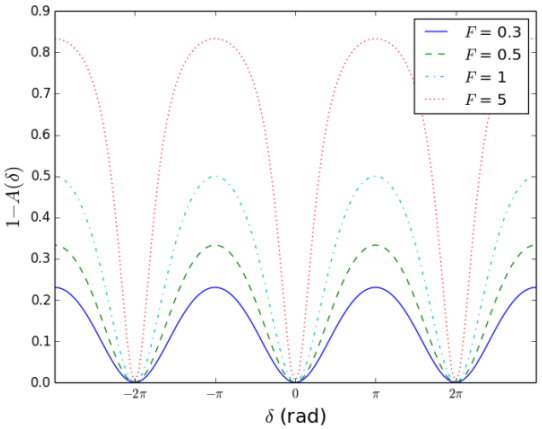

Fig. 2.3 Reflected spectrum of a low finesse FP interferometer, for different coefficients of finesse (F=0.3, 0.5, 1, 5).

2.2 Historical overview of fiber Fabry-Perot based sensors

Optical fiber sensors based on FP interferometry first breakthroughs happened for several decades. One of the first works published on the matter was carried out by Yoshino *et al.* [17], in 1982. The interferometer proposed consisted in a single mode fiber (SMF) with dielectric-coated high-reflectance end faces. Basic properties of the fiber interferometer were studied, among them are finesse, polarization and thermal response. This configuration was proposed as a sensor for temperature, mechanical vibration, acoustic waves, alternating current (AC) voltage, and AC and direct current (DC) magnetic fields.

In 1988, a simple pressure sensor was proposed [18]. The sensing head was composed by a SMF and a cavity was formed by the use of two mirrors. One of the mirrors was fixed, while the other was able to move due to pressure variations. In the Fig. 2.4 the sensing head proposed is presented.

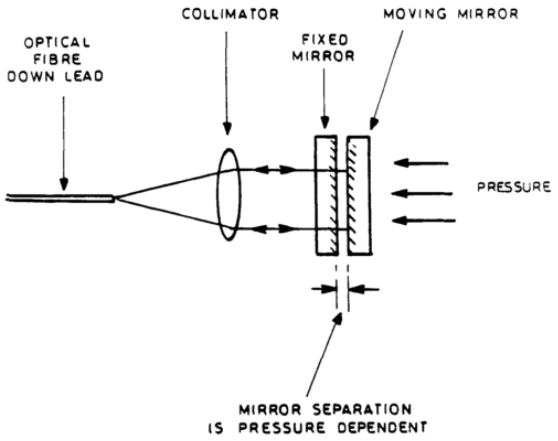

Fig. 2.4 Schematic diagram of the proposed sensing head [18].

A new FP configuration was proposed, in 1993, by Sirkis *et al.* [8]. The sensor was constituted by a hollow core fiber fusion spliced to two SMFs. The hollow core fiber had the same outer diameter as the optical fiber. This sensor was tested in dynamic strain, using a piezoelectric stretcher to induce strain variations. The sensor proposed is shown in Fig. 2.5. This novel sensor design was the impellor for the development of multiple sensors based on hollow core fiber.

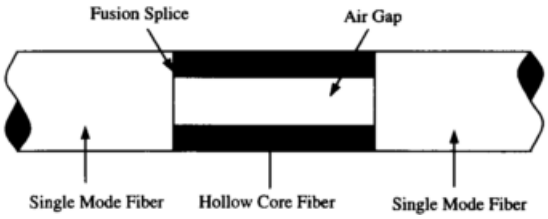

Fig. 2.5 Schematic diagram of the dynamic strain sensor [8].

In 1997, a magnetic field sensor based on a FP was proposed [15]. The sensor proposed was based on a FP interferometer formed between a cleaved SMF and a wire of Metglas ($Fe_{77.5}B_{15}Si_{7.5}$). The cavity was maintained using a hollow core fiber as encasement, where the tips of the Metglas wire and the optical fiber were fixed. An aluminum filament was used to fix the optical fiber tip as well as serving as a temperature compensator. This thermal compensation allowed a low magnetic field detection.

In 2000, a new frequency multiplexing for low finesse FP sensors was reported [19]. The concept was demonstrated by multiplexing three FP sensors in a tree topology and tested for strain and displacement. The accuracy achieved for displace measurements was 0.01 mm, with an estimated range of 1 mm. This system can be used to multiplex up to 20 FP sensors. In the same year, a sensor for blood vessel pressure monitoring in a catheter was reported [20]. The sensor head was constituted by a sensing element attached to the tip of a multimode fiber (MMF) resorting to a polyimide adhesive layer. The sensing element was fabricated by micromachining techniques. Both surfaces of light reflection were coated; the fiber tip was coated with zinc sulfide (ZnS) and the sensing element with aluminum. These coating allowed an increase of reflection light. The sensing head schematic is presented in Fig. 2.6.

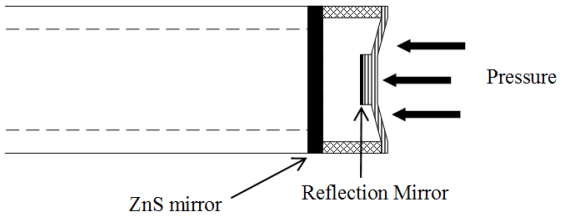

Fig. 2.6 Scheme of the sensing head. Adapted from [20].

In 2002 another blood pressure sensor was proposed [12]. The fabrication process was rather simple since only splicing and etching was needed. A SMF was fusion spliced to a MMF. Etching was carried out at the tip of the multimode fiber, using hydrofluoric acid. The diaphragm was formed simply by dipping the etched fiber in a solution of an elastic polymer in dimethyl formamid (DMF). The sensor was tested for pressure variations in the range of 0 to 300mmHg showing promising results.

Optical pressure sensors fabricated with etching processes were proposed in 2005, [13, 14]. In the same year, a diaphragm-based pressure sensor was also presented [21]. The proposed sensor didn't relied on etching for the formation of the cavity. Instead, an SMF and a diaphragm were fixed to a capillary tube, or hollow core fiber, trough bonding points. The all-silica structure presented advantages over ferrule-based sensors since, when temperature induced stress on the structure, the coefficient of thermal expansion was the same for all structure.

In 2006, pressure sensors with simpler structure were presented [22, 23]. A laser machined pressure sensor was proposed by Stuart Watson *et al.* [22]. An ArF excimer laser, operating at 193 nm, was used to ablate the air cavity on a SMF. The diaphragm was produced using an aluminized polycarbonate foil that, in contact to a UV curable epoxy, forms a thin membrane on the tip of the fiber. This process is shown in Fig. 2.7. Further work took place in multicore fiber, with a four-core fiber laser machined. In the present case, the fiber could be used for simultaneous detection of multiple parameters. Some fibers were coated to prove the possibility of measurement of pressure and temperature on adjacent cores. In Fig. 2.8, the four-core fiber ablated is shown. In the same year, a FP based sensor was proposed, consisting in a simple sensor tip for static pressure sensing [23]. The fabrication of the sensing head consisted on simply fusion splicing a hollow silica fiber between two cleaved SMFs. One of the SMFs was, then, cleaved with a short length serving as a diaphragm.

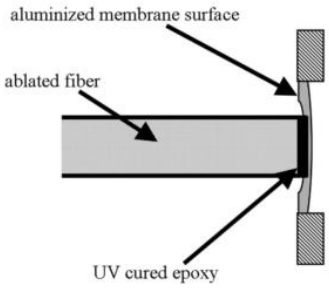

Fig. 2.7 Schematic of the diaphragm attachment procedure [22].

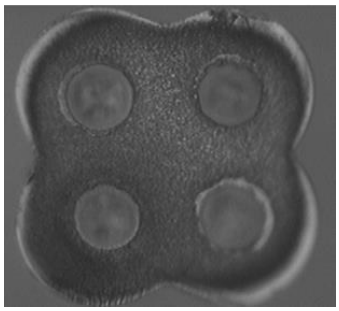

Fig. 2.8 Microscope photograph of the fiber with four cores ablated with 30 μm diameter cavities [22].

Hollow core photonic crystal fiber (PCF) based sensors were firstly introduced by Rao *et al.*, in 2007 [24]. The sensor was composed by a hollow core PCF, fusion spliced between two SMFs. A film of Ti_2O_3 was coated to the end surface of the lead-out fiber, as shown in Fig. 2.9 (a). The sensor was tested in strain and temperature. In 2010, the use of PCF was again proposed for refractive index measurements [25]. The sensor was fabricated using a hollow core fiber fusion spliced between an SMF and a PCF. In Fig. 2.9 (b), the structure is shown.

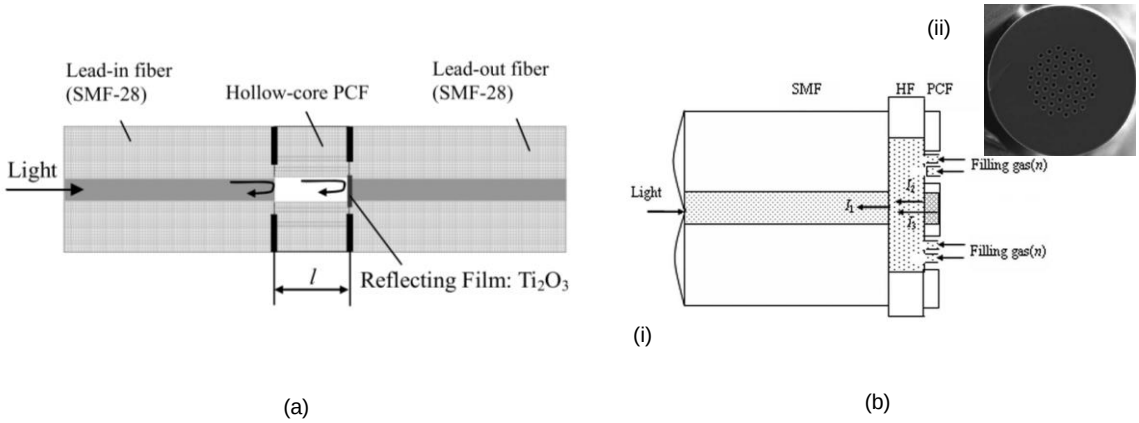

Fig. 2.9 - Sensor structure resorting to (a) a hollow PCF [24], and (b) a hollow fiber fusion spliced to a PCF [25]. In (b-ii) the PCF structure is shown.

The use of hollow core fibers was once again reported in literature, in 2011 [26, 27]. By using a hollow core silica tube, a newly sensor design was proposed [26]. The sensor was fabricated using a hollow core fiber, fusion spliced to a SMF. The sensor was tested in temperature and in refractive index. The simple design presented promising results. A similar design was used as the base for a new temperature and transverse load sensor [27]. After fusion splicing a hollow core fiber to a SMF, a second

electric arc was performed at the silica tube. This electric arc changes the structure of the hollow core fiber, resulting on the formation of a hollow microsphere at the tip of the sensing head. The sensor was tested for lateral loading and temperature. The process of fabrication of the microsphere is presented in Fig. 2.10.

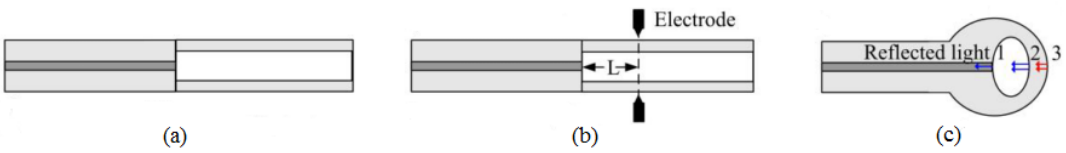

Fig. 2.10 Schematic of the microsphere formation process. (a) The hollow core fiber fusion spliced to a single mode fiber; (b) The place where the electric arc is performed; (c) The final structure. Adapted from [27].

Hollow core fiber based sensors continued to be a matter of research in 2012, where a simple in-line sensor for high intensity focused ultrasound fields detection was reported [28]. The proposed sensor consisted in a hollow core fiber fusion spliced between two SMFs. The proposed sensor design was easily reproducible since the only fabrication process needed was fusion splicing. In the same year, De-Wen Duan *et al.* [29], proposed a microbubble structure produced resorting only to fusion splicing. The cavity of the sensor is a microscopic air bubble, formed only by fusion splice. This fusion splicing was performed between two SMFs, one of them with a cleaved tip and the other with a hemispherical tip. In the Fig. 2.11, the fabrication procedure is shown.

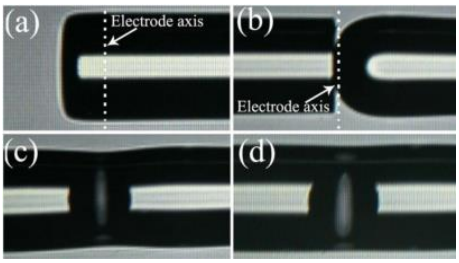

Fig. 2.11 Cavity fabrication steps [29].

In 2015, a silica capillary tube based sensor was reported [30]. The sensor, formed only by fusion splicing a hollow core fiber between a standard SMF and a side-hole fiber, whose microscope image can be seen in Fig. 2.12. The side-hole fiber allowed the entrance of gas to the cavity, varying the cavity pressure. The pressure variation induced a refractive index (RI) variation, making this sensor a promising solution for gas sensing applications. In the same year, a dual hollow core based sensor was proposed [31]. The presented sensor consisted a standard SMF fusion

spliced to a hollow core fiber. The fiber was, then, cleaved and fusion spliced to other hollow core fiber with a smaller inner diameter that allowed the entrance of liquids to the cavity. The tip of the hollow core fiber was cleaved with a small slope, preventing reflected light in the interface fiber/air. The sensor structure is presented in Fig. 2.13. The sensor was tested for thermo-optic coefficients, presenting a solution for measurements in liquids with volumes as low as 10^{-12}L.

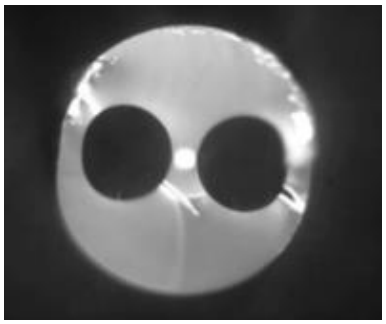

Fig. 2.12 Microscopic image of cross section of the side-hole fiber [30].

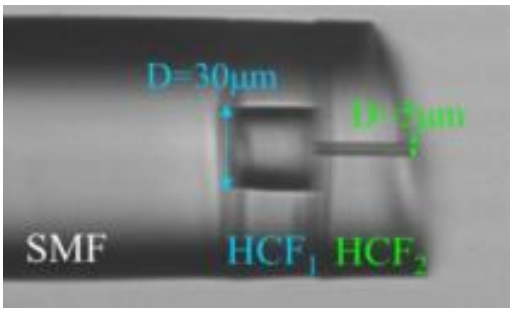

Fig. 2.13 Microscopic image of the sensor tip [31].

2.3 Concluding Remarks

The first Fabry-Perot based sensor in conventional optical fiber emerged in 1982. Since then, many different sensor structures were proposed for several sensing applications. In the last decade, microstructured fiber and silica capillary tubes are a matter of research for sensor fabrication.

Fabrication techniques have diversified over the years. Chemical etching, micromachining or laser ablation are some of the techniques proposed over the years. These techniques provide some solutions to obtain high sensitivity sensors. However, some of the structures are complex when several types of fiber are used in the same structure.

The use of microbubbles in order to produce an FP cavity is a matter of research in the recent years, for multiple physical parameters measurements. This fabrication technique is studied and developed over this dissertation.

Chapter 3

Curvature Sensor based on hollow core silica fiber

3.1 Introduction

Optical fiber sensors based on Fabry-Perot (FP) cavities are an interesting solution for engineering applications. Due to the small dimensions, they can be easily embedded in more advanced structures. The first FP cavities were fabricated in 1993, by splicing two standard single mode fibers (SMFs) with a silica capillary tube and tested for the measurement of dynamic strain [8]. Over the last decades, this type of interferometric sensor has been used for sensing a wide range of physical parameters such as temperature, vibration, pressure, and refractive index [26], [32–34]. A temperature sensor was proposed consisting of a tip of a single mode fiber coated with a thin film of polyvinyl alcohol [32]. The sensor provided a stable solution for temperature measurements, presenting a maximum sensitivity of 173.5 pm/℃ above 80℃. An all-fiber sensor based on FP interferometry was proposed for vibration measurements, showing insensitivity to environmental effects, along with the possibility of being embedded in composite material and used in harsh environments [33]. Refractive index is a key parameter for sensing purposes, and an FP-based sensing head formed by an air cavity was demonstrated [34]. In this case, the refractive index of gases was monitored as a function of pressure. An FP cavity based on a diaphragm-free hollow core silica tube was proposed [26]. The sensor head, composed by a hollow core silica tube spliced to a single mode fiber, was tested for pressure, refractive index, and temperature changes. The proposed sensor head was an interesting solution for both pressure and refractive index variations on fluids.

The optical fiber provides a great solution for curvature measurement purposes due to lightweight, compact dimensions, immunity to electromagnetic interference, and the resistance to corrosion. A curvature sensor based on a photonic crystal fiber was reported [35], showing a great sensitivity to the measurand and negligible sensitivity to temperature. Recently, a highly sensitive curvature sensor based on abrupt tapered fiber joined with a micro FP interferometer was presented [36]. The sensor head was sensitive only in visibility since the bending was applied before the FP cavity, not

affecting the optical path length. Optical fiber sensors for curvature sensing were already tested for medical purposes [37], where an optical sensor was used to sense the radius of curvature of a rotary endodontic file inside an artificial tooth root canal.

In this work, an FP cavity for curvature sensing is proposed. The sensor was produced by fusion splicing a capillary silica tube between two SMFs. The capillary tube had an outer diameter similar to the one of the single mode fiber and an inner diameter of 60 μm. Two FP sensors with different cavity lengths were tested in curvature and temperature and characterized in visibility and wavelength shift. Finally, the cross-sensitivity for both measurands was also analyzed.

3.2 Experimental Results

The experimental setup, shown in Fig. 3.1, is constituted by a broadband optical source, centered at 1550 nm and with a bandwidth of 100 nm, an optical circulator and an optical spectrum analyzer (OSA). The circulator provides interrogation of the sensing head in reflection and the OSA reads the spectral response of the sensing head with a resolution of 0.1 nm.

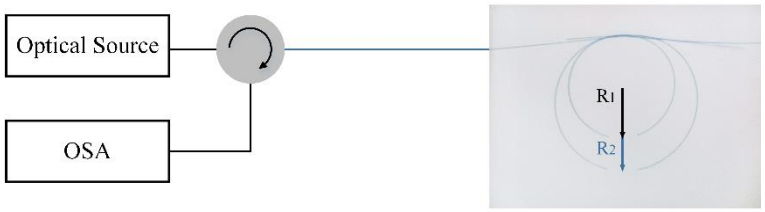

Fig. 3.1 - Experimental setup, with photograph of the curvature sensor with different curvature radii.

Two FP cavities with different lengths were characterized. The first sensing head has a cavity length of ~1154 μm and is called an FP-Long sensor, whereas the second one has a cavity length of ~508 μm and is called FP-Short sensor. Both cavities were produced using a hollow core silica tube with an inner diameter of ~ 60 μm, spliced between two SMFs. The arc discharge was performed with a splice machine in manual operation, where an offset of the capillary tube was applied to prevent its collapse. In Fig. 3.2, a scheme of the sensors used and a microscope photograph of the hollow core silica tube cross-section is presented.

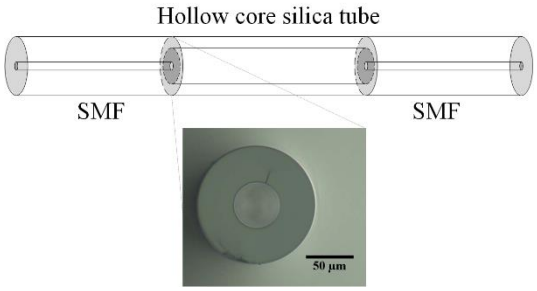

Fig. 3.2 - Scheme of the sensor heads and a microscope image of the hollow core silica tube cross-section.

The spectrum of the two sensor heads used is shown in Fig. 3.3. The FP-Long sensor presents a visibility of ~0.47 and has a free spectral range ($\Delta\lambda$) of ~1.04 nm. Regarding the FP-Short sensor, it has a visibility of ~0.41 and a free spectral range of ~2.40 nm. The light that is transmitted to the capillary tube travels mostly through the hollow core, which is filled with air. Refractive index of the optical cavity can be estimated using (3.1), where *n* is the refractive index and *L* the cavity length [9].

$$n = \frac{\lambda^2}{2L\Delta\lambda} \tag{3.1}$$

The refractive index of standard air at room temperature and atmospheric pressure was estimated and the result was approximately 1.0003 at the wavelength of 1550 nm, which goes according to the expected [38].The difference between obtained results and theoretical value of refractive index of air can be explained by possible errors committed while determining the cavity length due to software limitations.

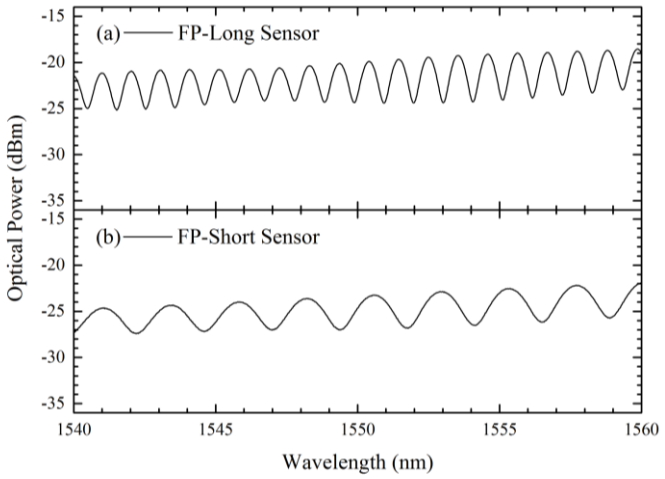

Fig. 3.3 - Reflection spectrum of (a) FP-Long and (b) FP-Short without curvature applied.

A curvature study was carried out using an overhand knot configuration, as depicted in Fig. 3.1. The position of the sensor head was maintained parallel to the position of the knot. A variation on the relative position of the sensing head produces a variation in visibility, while maintaining the position of the fringes of the spectrum. Fig. 3.4 (a) shows the spectral behaviour of the FP-Long when submitted to curvature. By stretching the fiber ends, the curvature radius diminished, resulting in the change in both visibility and wavelength as presented in Fig. 3.4 (a). The curvature radius was maintained large enough to ensure that the losses were reduced. The visibility of the sensor head decreased 20% because the reduction of the curvature radius diminished the coupling efficiency of the FP mirrors, while the wavelength shift was due to the variation of the optical cavity length. In the case of FP-Short, even though the wavelength shift is negligible, visibility decreases as curvature increases as depicted in Fig. 3.4 (b). The visibility diminishes 10% in the range of curvature studied, which is half of the value achieved in the FP-Long sensor.

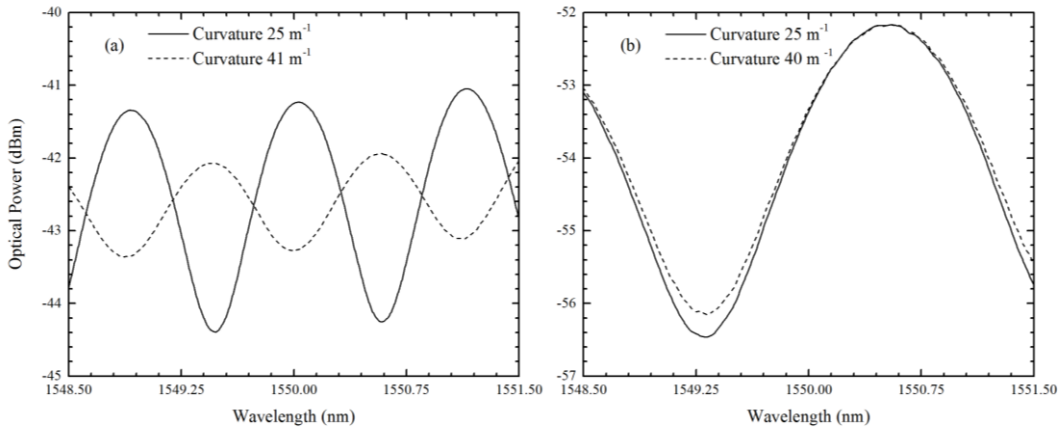

Fig. 3.4 - Optical reflective spectrum for different curvature radius of (a) FP-Long and (b) FP-Short sensor.

Fig. 3.5 shows the wavelength response of both sensing heads for different applied curvatures. The longer cavity, FP-Long, presented a non-linear response, but it is reasonable to divide the curvature range in three sub-regions where the response is linear. A sensitivity of 21.56±0.68 pm/m^{-1} was obtained for a high curvature radius, in the range of 45 m^{-1} to 55 m^{-1}. In the case of a lower curvature radius, between 25 m^{-1} and 35 m^{-1}, a sensitivity of 17.27±0.85 pm/m^{-1} was attained. A maximum sensitivity of 68.52±1.65 pm/m^{-1} was achieved for a curvature radius comprised between 35 m^{-1} and 45 m^{-1}.

The different regions of curvature response can be explained by the material behaviour to the curvature applied. In the region of 25 m^{-1} to 35 m^{-1}, the curvature radius applied to the sensor is not enough to curve the silica tube. Over this region, the spectral variation is due to compression over the interfaces caused by bending. On the other hand, over the region of 45m^{-1} to 55 m^{-1} the bend reaches a saturation point at which the silica tube stops bending. For higher curvature radius, the sensing head breaks at the splicing points.

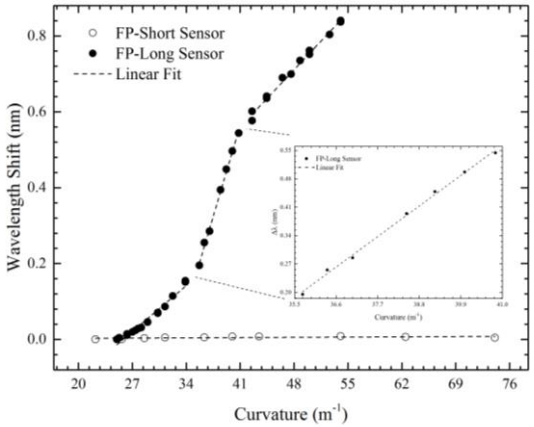

Fig. 3.5 - Curvature response of FP-Long and FP-Short (inset: detail of the curvature response of FP-Long over the region 35 m^{-1}- 45 m^{-1}).

Table 3.1 summarizes the curvature sensitivities for the considered ranges. Curvature was also applied to FP-Short using the knot method, resulting in a negligible sensitivity to curvature, as observed in Fig. 3.5, with a corresponding sensitivity of 0.09 pm/m^{-1}. The result is somehow expected, since the geometry of the FP-Short sensor is unchanged when curvature is applied, due to its small size. This implies that the optical path is independent of curvature changes.

Table 3.1 - Sensitivity for curvature of FP-Long sensor.

Cavity length (μm)	Range of measurement (m^{-1})	Sensitivity (pm/°C)
1140	25 – 35	17.27
	35 – 45	**68.52**
	45 – 55	21.56

Temperature response of both sensing heads were also studied. Each sensor was placed in an oven, where temperature varied from 30℃ to 80℃, with a resolution of 0.1℃. The FP-Long was characterized in temperature considering two different curvatures, namely, 23.5 m^{-1} and 50 m^{-1}, as presented in Fig. 3.6(a). The small wavelength change for the two different curvatures confirms the low sensitivity of the sensor to temperature, with sensitivities of 0.84 pm/℃ and 0.89 pm/℃, for 23.5 m^{-1} and 50 m^{-1} curvature radii, respectively.

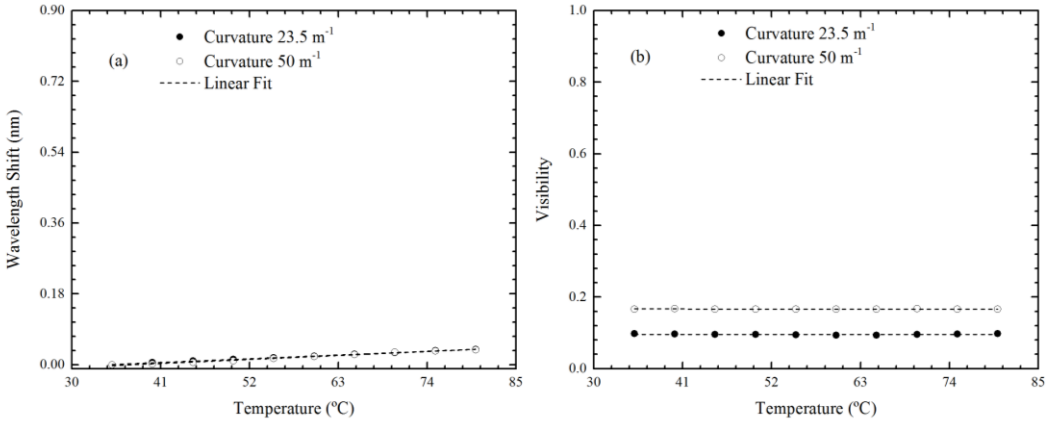

Fig. 3.6 - Temperature characterization for FP-Long submitted to 23.5 m^{-1} and 50 m^{-1} of curvature applied (a) in wavelength and (b) in visibility.

The FP-Short was also tested without any curvature applied, presenting a sensitivity of 0.83 pm/℃, as shown in Fig. 3.7 (a). In the present case, thermal expansion of the capillary tube is the main behaviour for the low temperature sensitivity. This feature presents an advantage over other similar reported sensing structures where attained temperature sensitivity was 20.6 pm/℃ [39]. The cross-sensitivity between curvature and temperature was also determined for the FP-Long sensor. Results of 0.052 m^{-1}/℃ and 0.041 m^{-1}/℃ for the lower curvature radius of 25 m^{-1} to 35 m^{-1} and higher curvature radius of 45 m^{-1} to 55 m^{-1}, respectively, were achieved. In the range of higher sensitivity to curvature a cross-sensitivity of 0.013 m^{-1}/℃ was also attained. For both sensor heads, visibility was almost constant throughout temperature variations, as depicted in Fig. 3.6 (b) and Fig. 3.7 (b).

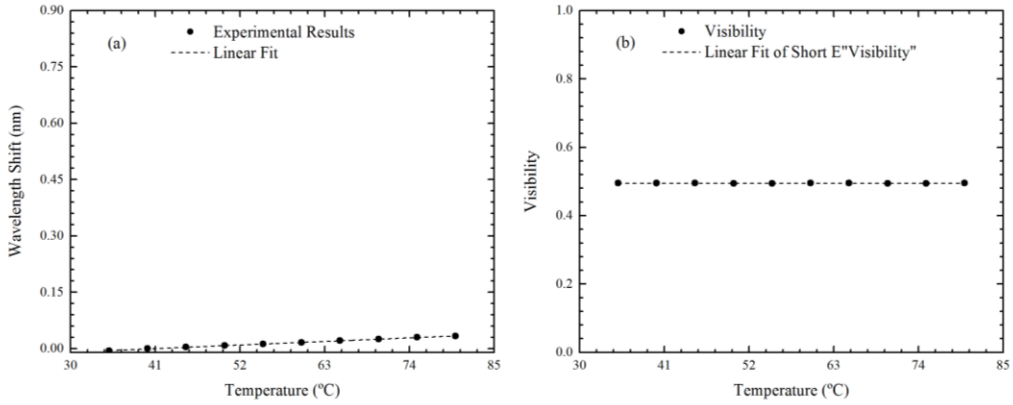

Fig. 3.7 - Temperature characterization for FP-Short sensor not submitted to curvature (a) in wavelength and (b) in visibility.

3.3 Conclusions

A curvature sensor based on an Fabry-Perot interferometer was demonstrated. Curvature and temperature responses were compared for two different cavity lengths. The sensing head with a longer cavity length (FP-Long) showed a non-linear response to curvature, presenting a sensitivity of 21.56 pm/m^{-1} at the low curvature region of 25m^{-1} to 35 m^{-1}, and 17.27 pm/m^{-1} at the curvature range of 45 m^{-1} to 55 m^{-1}. The FP-Long sensor presented a maximum curvature sensitivity of 68.52 pm/m^{-1}, in the range of 35 m^{-1} to 45 m^{-1}. For the FP-Long sensing head, the temperature response was studied, considering two different curvature radii, which led to the conclusion that curvature had low influence in the temperature response. Besides, the longer cavity exhibited negligible sensitivity to temperature, presenting a maximum cross-sensitivity of 0.052 $m^{-1}/°C$. The smallest cavity (FP-Short) showed low sensitivity to the parameters studied, providing an alternative solution to measure others physical parameters. The proposed configuration can be easily adapted in pipeline with curvature radii between 0.04 m (1.58 inches) and 0.02 m (0.79 inches).

Chapter 4

Fiber-tip sensor based on a hollow microsphere cavity

4.1 Introduction

Several pressure sensors based on fiber Fabry-Perot interferometry are already published in the literature. It has been extensively investigated and applied to numerous areas such as biomedicine and biomechanics [3, 40] and civil engineering [41]. The main concern on this subject is that some of the proposed pressure sensors rely on rather expensive fabrication processes such as micromachining or through etching processes [12, 14, 20, 42]. This fabrication processes, besides being expensive, are not easy nor they are eco-friendly since some of the processes (e.g. wet etching) rely on chemicals that are harmful to the environment.

Sensor fabrication using low cost techniques emerged as an alternative to the previous developed techniques. In 2011, Jun Ma *et al.* [27], proposed a sensor fabricated only using a fusion splicer. The electric arcs performed on the tip of a silica capillary built up a hollow microsphere at the tip of the sensor, resulting on a three-wave interferometer. The sensor was tested for lateral loading, resulting in a maximum sensitivity of 1.37 nm/N. It also presented a low temperature dependence, achieving a sensitivity of 2.1 pm/°C. In 2014, Changrui Liao *et al.*, proposed a gas pressure sensor [43]. The fabrication technique is similar to the previous demonstrated. The hollow microsphere is positioned at the tip of the sensor, reaching a minimum diaphragm of ~320 nm. The sensor, tested for gas pressure and temperature, resulted in a high pressure sensitivity and a low cross-sensitivity to temperature.

In this work, a hollow microsphere tip sensor proposed. The fabrication techniques rely only in fusion splicing processes. Three sensor heads were fabricated and tested for lateral loading and temperature.

4.2 Sensor fabrication and operation principle

4.2.1 Sensor Fabrication

The sensor fabrication steps are shown in Fig. 4.1. The sensor fabrication relies only on cleaving and fusion splicing processes, and involves two steps. The first step, as shown in Fig. 4.1(a) and Fig. 4.1(b), consisted in a standard single mode fiber (SMF) fusion spliced to a hollow core silica fiber. The electric arc, performed in a manual program (program 1, present in Table 4.1), is centered on the top of the SMF. This prevents the hollow core fiber to deform or collapse with the heat, while being able to join the SMF to the hollow core fiber. This process is pictured in Fig. 4.1(a). After splicing, the tip of the fiber is cleaved as shown in Fig. 4.1(b).

In the second step, pictured in Fig. 4.1(c) and Fig. 4.1(d), a different splicing program is used (program 2, present in Table 4.1). In this process, two electric arcs are performed at the tip of the hollow core fiber. The first arc collapses the capillary tube, resulting in a microsphere with thick silica walls (see Fig. 4.1(d)). The second electric arc results in a microsphere with thinner walls. The resulting structure is shown in Fig. 4.2. The fusion splice program parameters are summarized in Table 4.1.

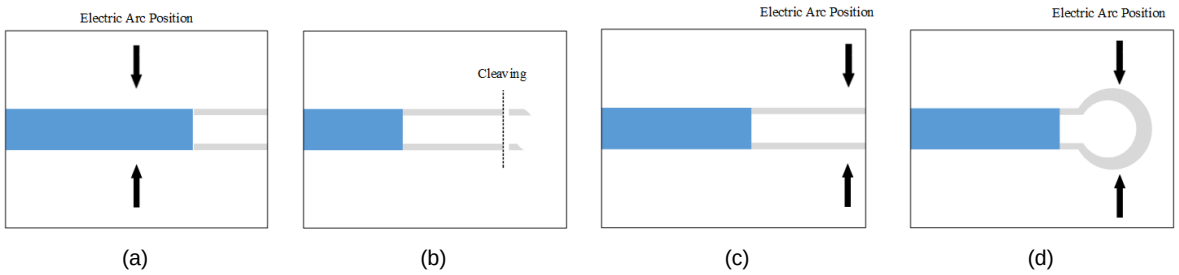

Fig. 4.1 - Schematic diagram of the fabrication process of the FPI sensor using electrical arc discharge and cleaving.

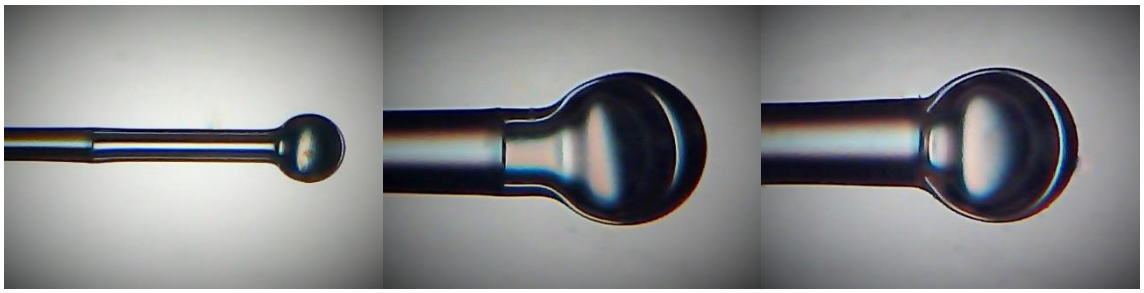

Fig. 4.2 – Microscope photograph of the sensor structure after the fabrication process: (a) Sensor 1, (b) Sensor 2, and (c) Sensor 3.

Table 4.1 – Splicing programs parameters

Parameter	Program 1	Program 2
Pre-fusion Time (s)	0	0
Fusion Time (ms)	300	2000
Arc Power*	S-075	S+100

* Absolute arc-power was not possible to obtain; only relative values were attained (S being the standard value)

4.2.2 Operation Principle

The sensor head schematic diagram is shown in Fig. 4.3. The light that goes through the SMF is partially reflected at the interface fiber/air, corresponding to reflection 1. Usually only around 4% of the light is reflected. The light that reaches the air cavity is going to be reflected at the interface air/silica, corresponding to the reflection 2. The portion of the light that goes through the silica wall is, again, partially reflected on the interface silica/air, marked as reflection 3.

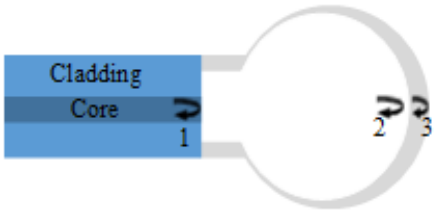

Fig. 4.3 - Schematic representation of the sensor principle of operation.

The reflected spectrum is the result of the interference between the three reflected waves (1, 2 and 3). The reflected intensity is given by the following expression [44]:

$$I(\lambda) = I_1 + I_2 + I_3 - 2\sqrt{I_1 I_2}\cos(\phi_1) - 2\sqrt{I_2 I_3}\cos(\phi_2) + 2\sqrt{I_1 I_3}\cos(\phi_1 + \phi_2) \quad (4.1)$$

Where I_1, I_2 and I_3 are the reflected waves intensity; ϕ_1 and ϕ_2 the phase shift that occurs in the interface air/glass and glass/environment, respectively, and are given by:

$$\phi_1 = \frac{4\pi}{\lambda} n_{air} L_{air} \qquad \phi_2 = \frac{4\pi}{\lambda} n_{silica} L_t \tag{4.2}$$

Where L_{air} is the air cavity length and L_t the outer silica wall thickness. An analysis of the structure geometry allows the simulation of the sensor spectrum. Through the simulation is possible to determine parameters of the given sensor such as the reflectivity of the surfaces.

The spectrum of the sensor 1 was normalized and is presented in Fig. 4.4. The simulated spectrum presented a similar shape to the attained experimentally. This simulation enabled to understand that the influence of the interference between R_2 and R_3 is negligible.

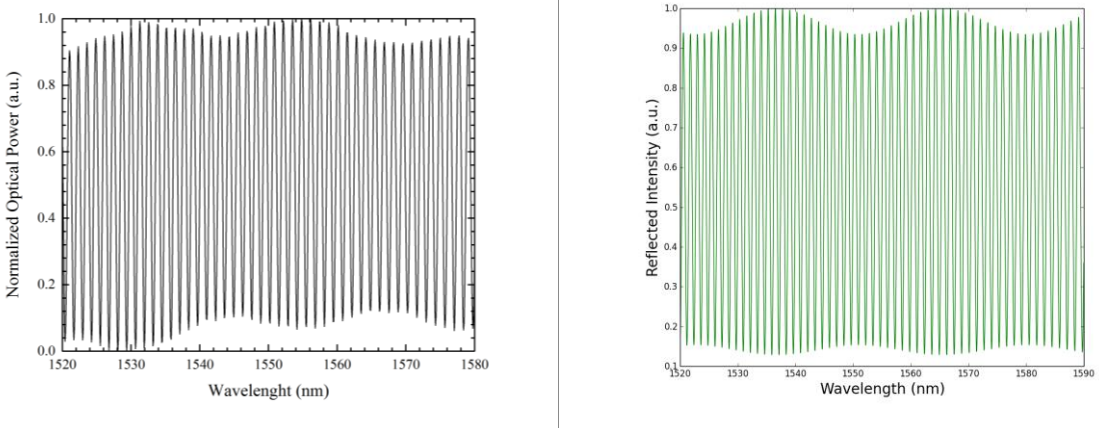

Fig. 4.4 - Spectrum of Sensor 1: (a) experimental and (b) simulated.

Further proof that the interference between R_2 and R_3 can be negligible can be found in the Fast Fourier Transformed (FFT) of the experimental spectrum. In the Fig. 4.5, the signal FFT is presented. Only two representative picks can be found, and are respective to the cavities 1 and 3, with L_1 and L_3.

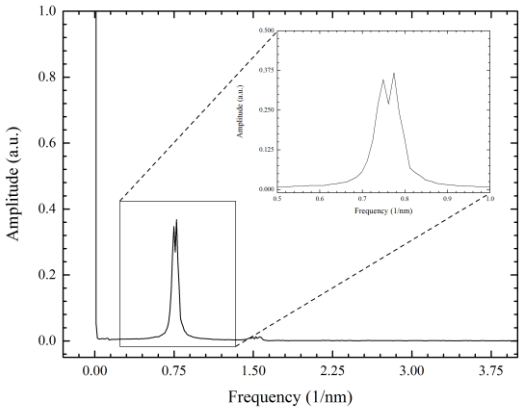

Fig. 4.5 - FFT of the experimental signal, for Sensor 1.

The normalized spectrum and the simulated signal of the sensor 2 is presented in Fig. 4.6. The simulated spectrum shows a similar form as the experimental attained. The differences between the two can be explained by the optical losses due to the cavity geometry. The FFT of the experimental signal, shown in Fig. 4.8 (a), proves that the influence the interference between $R_2$and R_3 is, again, negligible.

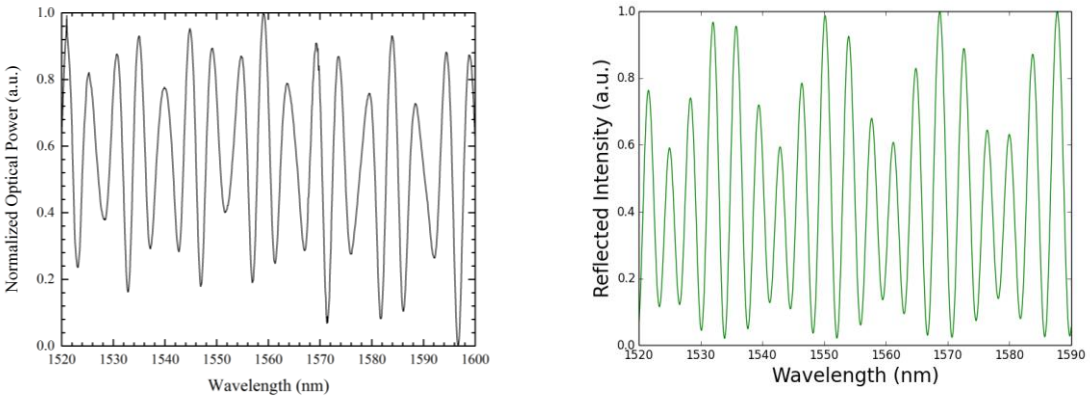

(a)

(b)

Fig. 4.6 - Spectrum of Sensor 2: (a) experimental and (b) simulated.

In the Fig. 4.7, the normalized reflected spectrum of the sensor 3 is show. The simulated spectrum presents the same form as previously demonstrated. The FFT, in the Fig. 4.8 (b), shows that the cavities 1 and 3 are dominant in the interference process, even though the relevance of the cavity 2 increases. This happens due to the relative sizes of the cavity. In the case of the sensor 3, the dimensions of the silica cavity start to be comparable to the air cavity.

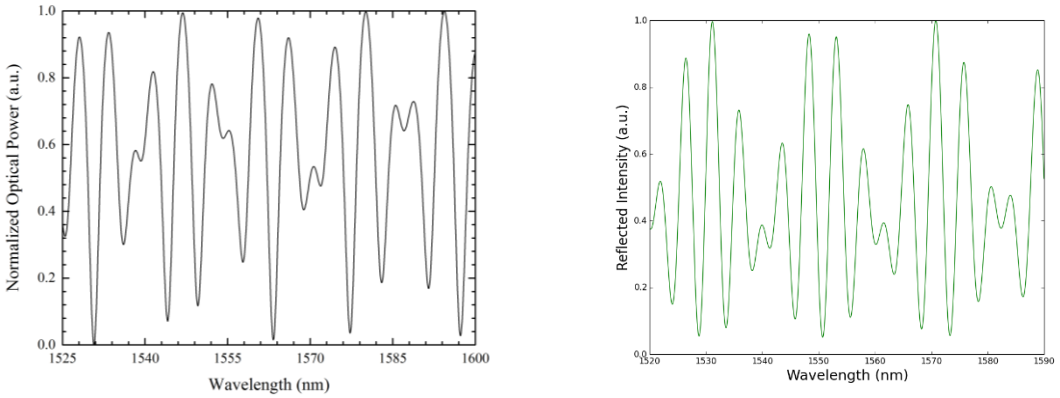

(a) (b)

Fig. 4.7 - Spectrum of Sensor 3: (a) experimental and (b) simulated.

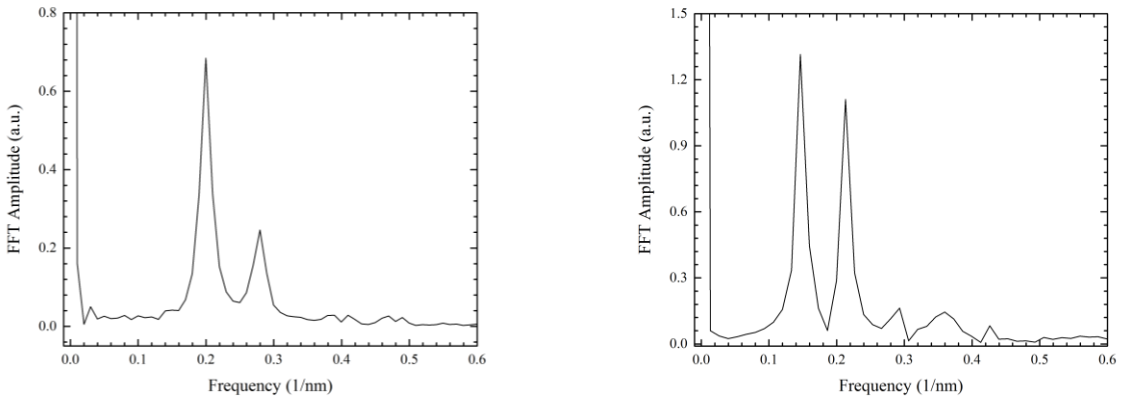

(a) (b)

Fig. 4.8 – FFT of the experimental spectrum of the (a) Sensor 2 and (b) Sensor 3.

4.3 Experimental Results

The experimental setup used to characterize the proposed sensors is illustrated in Fig. 4.9. A broadband source, with 100 nm bandwidth and centered at 1550 nm, is connected to the sensor and to the optical spectrum analyzer (OSA) through an optical circulator. The optical circulator serves as the interrogation system for the reflected signal.

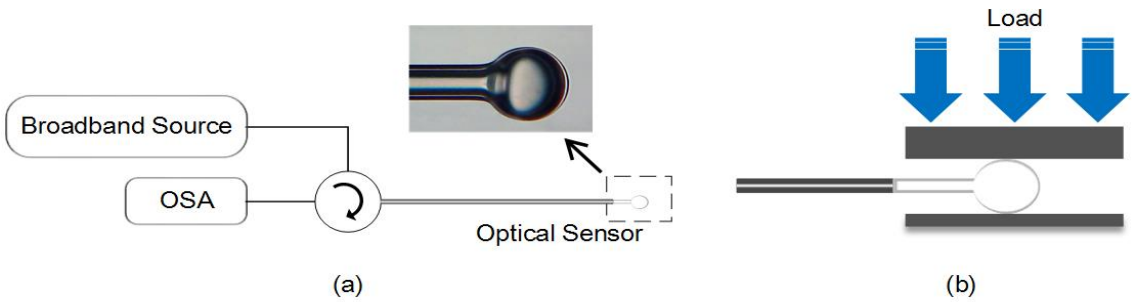

Fig. 4.9 – (a) Experimental setup and sensing head microscope image. (b) Lateral loading setup.

4.3.1 Lateral Loading

Lateral loading tests were carried out in the three fabricated sensors, using the experimental setup depicted in Fig. 4.9 (b). The spectral behaviour of the three sensors is similar, presenting a variation in wavelength while maintaining the optical power. The lateral loading responses for the three sensors are shown in Fig. 4.10. A sensitivity of 0.514 ± 0.005 nm/N was obtained for Sensor 1 and for Sensor 2 a sensitivity of 1.03 ± 0.02 nm/N was attained. A maximum sensitivity was found for Sensor 3 obtaining a sensitivity of 1.56 ± 0.01 nm/N. The maximum sensitivity is higher than the previous 1.37 nm/N sensitivity reported in [27].

Table 4.2 – Lateral loading sensitivity

Sensor	Sensitivity (nm/N)	Δλ (nm)
1	0.514 ± 0.005	1.36
2	1.03 ± 0.02	5.50
3	**1.56 ± 0.01**	**5.48**

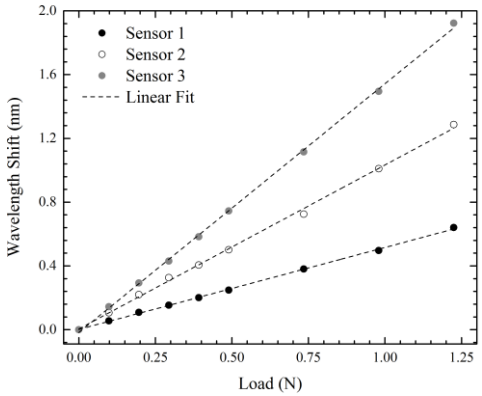

Fig. 4.10 - Lateral loading responses for the three sensors.

4.3.2 Temperature

Thermal behaviour of the sensing heads was also studied. Sensor 2 was placed in an oven with temperatures in the range of 250 to 550 ºC, measured with a resolution of 0.5ºC. Thermal variations cause a thermal expansion of the hollow sensor tip, varying the cavity length. Temperature response of the Sensor 2, shown in Fig. 4.11, indicates a nonlinear wavelength shift, on the tested range. For high temperatures, between 300 and 500 °C, the behaviour can be approximated to a linear response, with a sensitivity of 1.90±0.06 pm/°C, with a $r^2 = 0.99$.

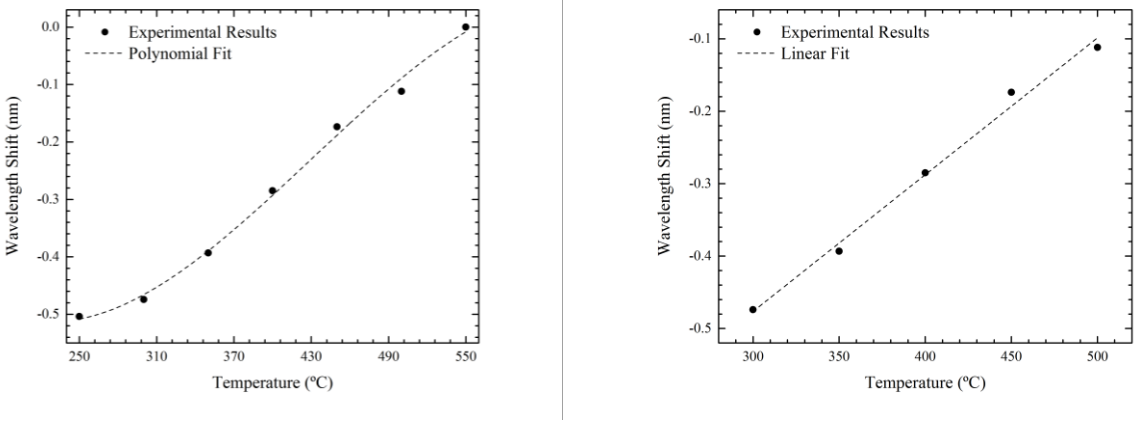

Fig. 4.11 - Temperature response of Sensor 2. On the left, the response through all the studied range with the polynomial fit curve. On the right is presented the range where the behavior is approximatively linear, accompanied with the respective linear fit.

4.4 Conclusions

An all-silica tip sensor based on Fabry-Perot interferometry to lateral loading measurements was proposed. The sensor was composed by a single-mode fiber and hollow microsphere tip. The fabrication of the sensor relied only in cleaving and fusion splicing techniques that allowed the deformation of the hollow core fiber into a microsphere tip. Three sensors were fabricated using the same method and were tested for lateral loading response. The sensor with a smaller cavity length achieved a maximum sensitivity of 1.56 nm/N, for loadings comprised between 0 and 1.25 N. The obtained sensitivity is higher than the reported in the literature, where a similar sensor structure was proposed. One of the sensor was also studied in thermal response, proven low temperature sensitivity. This result was expected due to the sensor all-silica composition. The proposed sensor resulted in higher lateral loading, with very low thermal dependence, suitable for hash environments applications.

Chapter 5

Fabry-Perot sensor based on two coupled microspheres

5.1 Introduction

All-silica Fabry-Perot optical fiber sensors have proven to be a great solution for harsh environments measurements due to small temperature sensitivity, with all the inherent benefits to the use of optical fiber in sensors. One of the proposed solutions is the formation of spheroidal microcavities inside of the sensor. This can be achieved by using fabrication techniques that usually rely on chemical etching [45], femtosecond laser micromachining [46] and hollow core photonic crystal fiber (HCPCF) [47]. These fabrication techniques can be expensive or complicated and, in the case of HCPCF based sensors, rely on rather expensive fibers.

Fusion splicing based sensors emerged as an alternative to the more expensive techniques. In 2011, De-Wen Duan *et al.* [29], proposed a microbubble based sensor for strain measurements, achieving a 4 pm/με sensitivity with a low thermal sensitivity of 0.9 pm/°C. In 2014 two all-silica sensors with very different structures were published [48, 49]. One of the proposed sensors was fabricated with an air spheroidal cavity and was tested, again, for strain [48]. The sensor presented a higher sensitivity of 6 pm/με, registering once more low thermal sensitivity. The proposed sensor by Ai Zhou *et al.* [49], had a very different approach. This sensor had two FP air cavities, one spheroidal cavity fusion spliced to a hollow core fiber, the structure is presented in Fig. 5.1. The sensor was tested for simultaneous measurements of strain and temperature, achieving sensitivities of 5.2 pm/με and 1.3 pm/°C for the air cavity and 1.1 pm/με and 13 pm/°C in the silica cavity, respectively. The different sensitivities allow the simultaneous determination of the measurands.

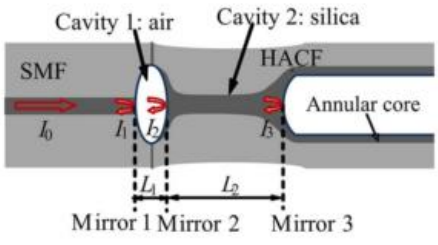

Fig. 5.1 - Sensor structure proposed by Ai Zhou *et al.* [49].

An array of solid microspheres was recently proposed by in the literature [50]. The proposed sensor, fabricated only through fusion splicing techniques, was tested for strain and temperature. Three different sensors were tested with arrays ranging from two to four. A maximum sensitivity of 1.59 pm/με was achieved for the three microspheres' structure. Thermal response was tested, obtaining a ~20 pm/°C sensitivity, a value independent of the sensor structure.

In this chapter, a sensor based on two hollow spheroidal cavities is proposed. The sensor is fabricated by fusion splicing a SMF to a hollow core fiber and, by applying two more intense electric arcs, a hollow spheroid is formed at the tip of the sensor. Two similar structures are fusion spliced, forming an in-line transmission sensor. Four sensors with cavity parameters are tested for strain response. One of the sensors is, then, tested for curvature and temperature. Despite having a similar structure, the proposed sensor can be used for monitoring parameters that couldn't be accessed using the previous proposed configuration. The possibility of measuring strain and curvature constitutes the main advantage of the proposed sensor, in this chapter.

5.2 Sensor Design and Spectral Characteristics

The sensor fabrication is schematized in Fig. 5.2. Two sensors are produced using the same fabrication steps demonstrated in Chapter 4, depicted in Fig. 4.1. Using a manual splicing program (named program 3, present in Table 5.1), the two sensors are joined. The programs parameters are listed in Table 5.1.

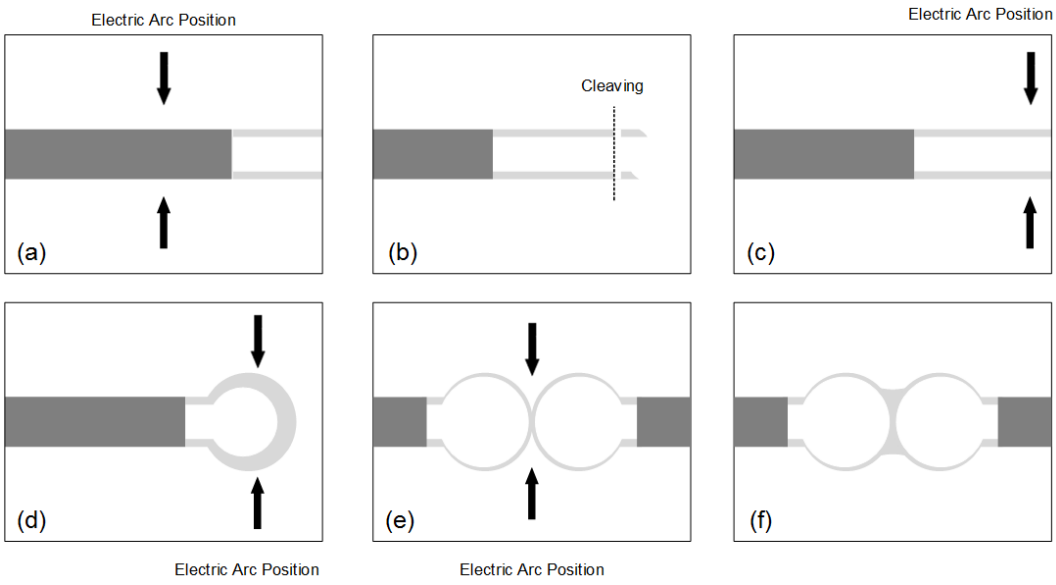

Fig. 5.2 - Schematic diagram of the fabrication steps.

Table 5.1 – Splicing programs parameters

Parameter	Program 1	Program 2	Program 3
Pre-fusion Time (s)	0	0	0
Fusion Time (ms)	300	2000	600
Arc Power*	S-075	S+100	S-050

* Absolute arc-power was not possible to obtain; only relative values were attained (S being the standard value)

The sensor's readings were attained in transmission. The resulting signal is the outcome of four wave interference. In Fig. 5.3, the reflecting scheme is presented.

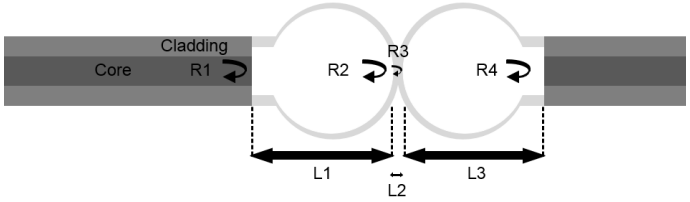

Fig. 5.3 - Reflection scheme of the proposed sensor.

The transmission intensity is given by [51]:

$$\frac{I_t}{I_i} = \frac{T^4}{D} \tag{5.1}$$

Assuming that all interfaces have the same reflectivity, the denominator, *D*, is:

$$\begin{aligned} D = {} & 1 + 6R^2 + R^4 \\ & + 2R[\cos(\phi_1 + \phi_2 + \phi_3) \\ & + R\cos(\phi_1 - \phi_2 - \phi_3) \\ & + R\cos(\phi_1 + \phi_2 - \phi_3) + R^2\cos(\phi_1 - \phi_2 + \phi_3)] \\ & + 4R^2[\cos(\phi_1 + \phi_3) + \cos(\phi_1 - \phi_3)] \\ & + 2R(1 + R)[\cos(\phi_1 + \phi_2) + \mathrm{R}\cos(\phi_1 - \phi_2) \\ & + \cos(\phi_2 + \phi_3) + \mathrm{R}\cos(\phi_2 - \phi_3)] \\ & + 2R(1 + R)^2[\cos\phi_1 + \cos\phi_2 + \cos\phi_3] \end{aligned} \tag{5.2}$$

Where R is the reflectance of the surfaces, $\phi_{1,2,3,}$ are the phase differences of the waves, in cavity 1, 2 and 3 respectively, given by:

$$\phi_1 = \frac{4\pi}{\lambda_0} n_{air} L_1 \qquad \phi_2 = \frac{4\pi}{\lambda_0} n_{silica} L_2 \qquad \phi_3 = \frac{4\pi}{\lambda_0} n_{air} L_3 \tag{5.3}$$

5.3 Experimental Results

The interrogation system consisted in a simple transmission setup, constituted by a broadband source and an optical spectrum analyser (OSA). The optical source has a bandwidth of 100 nm, centered at 1550 nm. The transmission data was acquired with a resolution of 0.5 nm. The fabricated sensors were tested in strain and curvature responses.

5.3.1 Strain Response Tests

The spectra of the sensors tested in strain are shown in Fig. 5.4, and the respective microscope images are also presented. Strain testing was carried out by holding one end of the sensor while the other was attached to a translation stage, with a resolution of 0.01 mm. By tracking one of the peaks of each spectrum, strain measurements were done for the four different sensors. All the tested sensors presented a linear response in wavelength. One of the sensors was tested for a wider range of strain, between 0 and 2000 με. The response of this sensor is present in Fig. 5.5 (a). Three other sensors were tested for a narrower range of 400 με to prevent the sensors from fracture in the joining position. The sensors' responses are shown in Fig. 5.5 (b), presenting, once more, a linear behaviour. The Sensor 3 was tested for a broader range, presenting two linear response regions, both summarized in Table 5.2.

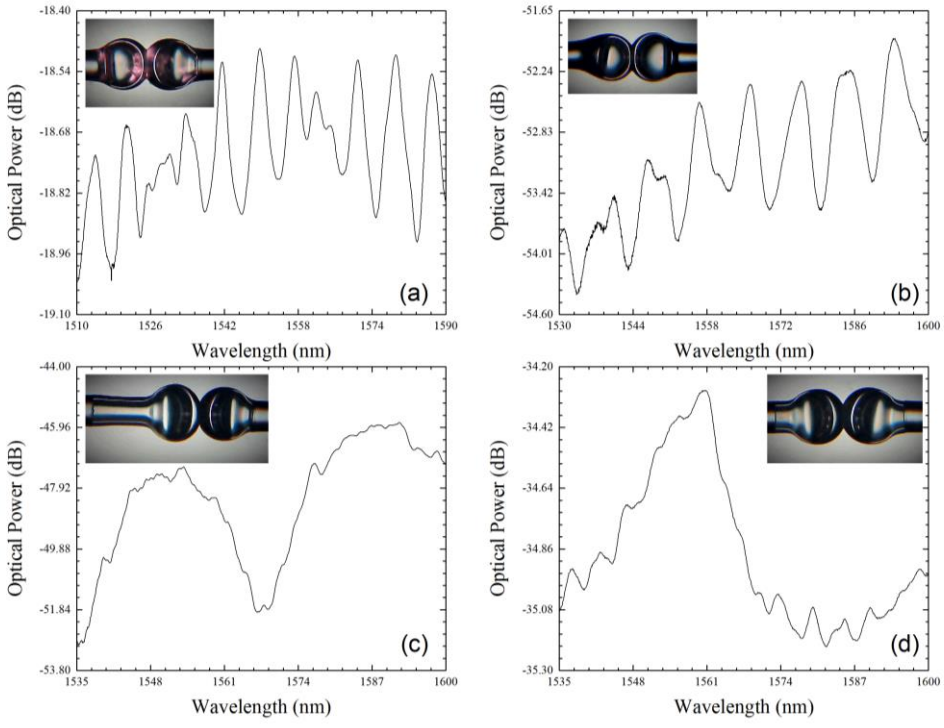

Fig. 5.4 - Transmission spectrum of (a) Sensor 1, (b) Sensor 2, (c) Sensor 3, and (d) Sensor 4.

All sensors sensitivities are gathered in Table 5.2.

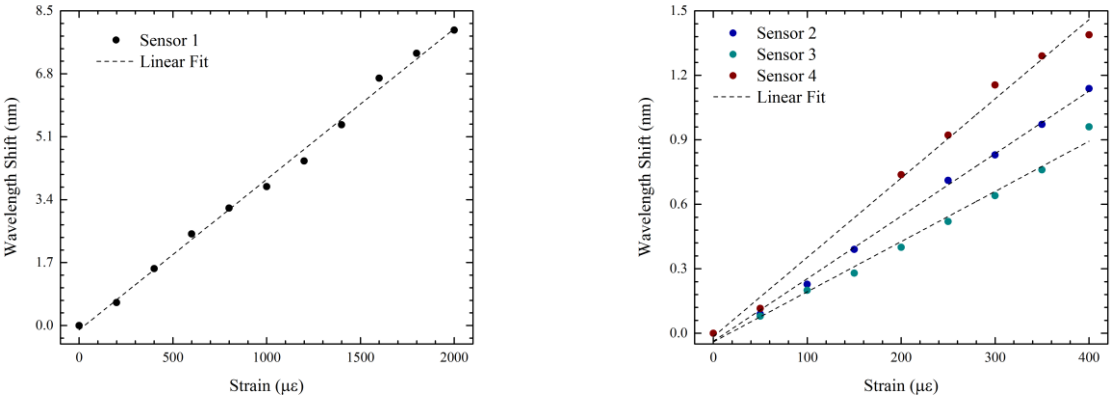

(a) (b)

Fig. 5.5 - Sensors response to the applied strain in (a) Sensor 1 and (b) in sensors 2, 3, and 4.

Table 5.2 – Strain sensitivity

Sensor	Sensitivity (pm/με)	Range (με)	Δλ (nm)
1	**4.07 ± 0.09**	0 – 2000	8.16
2	2.91 ± 0.06	0 – 400	9.38
3	2.33 ± 0.09	0 – 400	35.90*
	3.68 ± 0.09	400 – 600	
4	**3.7 ± 0.1**	0 – 400	**

*Estimated value.
**Value not possible to attain using the studied range of wavelengths.

The maximum achieved sensitivity, for Sensor 1, was more than four times the sensitivity obtained for the sensor proposed in [50], for the sensor with 2 microspheres, which presented a − 0.87 pm/με sensitivity. From the proposed sensors in the paper, a maximum sensitivity of − 1.59 pm/με was achieved for the sensor with 3 microspheres, which is more than 2.5 times smaller than the obtained in this work.

5.3.2 Curvature Response Tests

Curvature response was tested for sensor 4, previously presented. By fixing one end of the sensor and attaching the other to a translation stage the curvature was applied to the sensor. The experimental setup is present in Fig. 5.6. The curvature is given by:

$$C = \frac{1}{r} = \frac{2h}{h^2 + (L + \Delta L)^2} \tag{5.4}$$

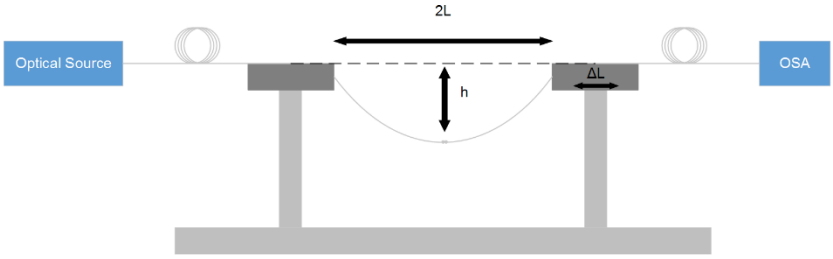

Fig. 5.6 - Setup used for curvature testing.

The joint place was kept in the point of maximum curvature, at the midpoint between the fixed points. The curvature was varied between 0 and 1.56 m^{-1}, with an initial distance (*2L*) of 16 cm. The spectral variation was only observed in optical power, maintaining the original position of the fringes. The sensor's response, in Fig. 5.7, is linear and a sensitivity of 0.145 ± 0.007 dB/m^{-1} was achieved for a central wavelength of 1561 nm.

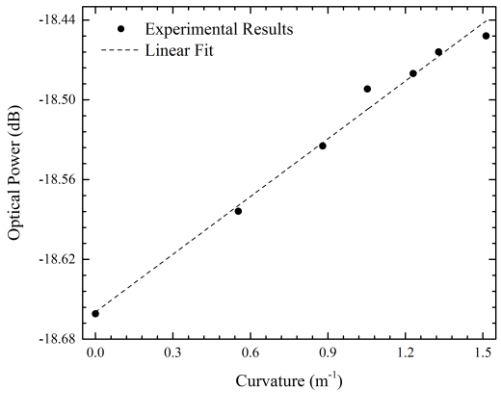

Fig. 5.7 - Optical power response for applied curvature, for sensor 4.

The invariance of the fringe positions could be explained by the low applied curvature not being enough to produce a significant deformation on the cavity. However, the applied curvature was enough to increase the coupling efficiency between the two hollow microspheres.

5.3.3 Temperature Response

The sensor response to temperature was, also, studied in the Sensor 1. The temperatures studied were between 200 and 550 °C. Thermal variations gave rise to a wavelength shift due to variations in the cavities length. The sensor's response, presented in Fig. 5.8, shows a positive wavelength shift tendency. Even though the response is not very stable, a sensitivity can be determined. For the studied sensor, a sensitivity of 2.4 ± 0.3 pm/°C was achieved.

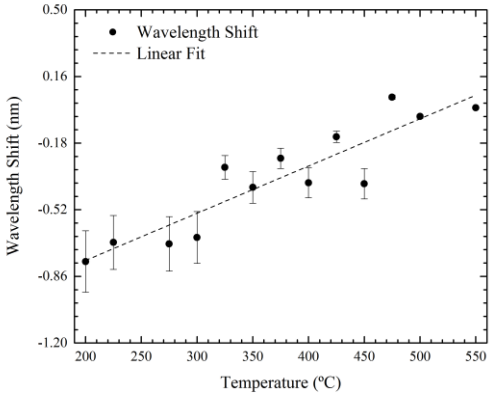

Fig. 5.8 - Temperature response of the Sensor 1.

The achieved result is around 10 times lower than the reported in literature [50], where an array of all-silica microspheres were proposed. The reported sensors achieved sensitivities of ~20 pm/°C for all the different structures proposed. In the present case, the cavities are less sensitive to thermal variations due its composition. The response instability may be due the resolution of the OSA or to structural stresses in the cavity, resulted in the fabrication process.

5.4 Conclusions

To summarize, four sensors with two hollow microspheres were fabricated using only fusion splicing techniques. The produced sensors are an all-silica, fusion splice based sensor. The easy and fast production process makes this solution easily reproducible.

Strain response was acquired showing a linear response, and a high sensitivity was also attained for all sensors. The maximum strain sensitivity of 4.07 pm/με was achieved. This maximum sensitivity is more than four times the maximum sensitivity obtained previously for a two microspheres structure proposed in the literature.

One of the fabricated sensors was also tested for curvature. The applied curvature gives rise to an optical power shift, while maintaining the position of the fringes. The sensor presented a linear response with a sensitivity of 0.145 dB/m^{-1}. Despite the fact that the sensor does not present a high sensitivity, the wavelength insensitivity can be an advantage for strain measurements in non-stretched surfaces.

Thermal response was, likewise, attained for one of the sensors. The tested sensor showed a linear tendency, with a sensitivity of 2.1 pm/°C. The low thermal sensitivity is due to the sensor configuration and can be an advantage over thermal sensitive sensors for applications in harsh environments.

This configuration allows the measurement of strain and curvature, two measurands that could not be attained by the use of the previously proposed sensor in Chapter 4.

Chapter 6

3D printed structure for embedding optical sensors

6.1 Introduction

The development of the first 3D printer took place in the 1980's. Easy, fast and low cost production of prototypes was the main impellor for the expansion of the three dimensional printing, or additive manufacturing. In the early stages of development, 3D printers were used to reproduce concept models, vastly used in civil engineering – a process called fast prototyping. Since then, 3D printing has found a wide variety of applications, ranging from arts [52], engineering [53] and medicine [54].

In the recent years, three dimensional printing has found promising applications in sensing industry. 3D printing allows the production of embedded sensors through a method named embedded 3D printing (e-3DP), and it allows the production of miniaturized sensors, easily reproducible, at a low cost. It has already been tested for bending [55], strain [56] and there are already commercially available products with sensors produced that use 3D printing.

The advances in optical fiber based sensors resorting to three dimensional printing recent and it is a promising area for further developments. Three different optical sensors were proposed recently, two based on FBG for strain [57] and pressure sensing [58], and one based on a Fabry-Perot cavity for vibration sensing [59].

In this chapter, three microsphere based sensors are embedded in a 3D printed structure. The embedding structure is similar for all the sensors, varying only in height of the surrounding structure, while maintaining the remaining geometries parameters. The three sensors are tested for lateral loading and temperature, and its resolutions are attained.

6.1.1 Recent developments on 3D printed sensors

A strain sensor, embedded in a 3D printed structure, was proposed by Michal G. Zubel, *et al.* [57]. The proposed sensor was tested for both strain and temperature, and it was the first 3D-printing embedded polymer optical fiber Bragg grating (POFBG) reported. It presented a repeatable strain sensitivity of 0.38 pm/με, with an instability for temperature, obtaining a sensitivity ranging from 30 to 40 pm/°C. The structure the sensor is presented in Fig. 6.1.

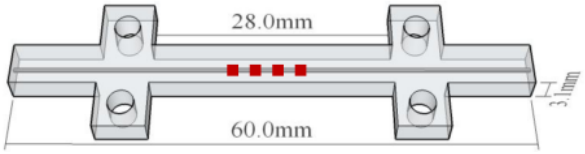

Fig. 6.1 - 3D printed structure, located inside the POFBG [57].

An optical fiber Bragg grating embedded in a 3D printed packaging for pressure sensing was proposed by Ying-Kai Lin, *et al.* [58]. The sensor was tested for pressure between 0 and 4 bars, using a static water tank. Further simulations were carried out to confirm experimental results. A sensitivity of 0.208 nm/bar was achieved. In the Fig. 6.2, the structure of the pressure sensor is presented.

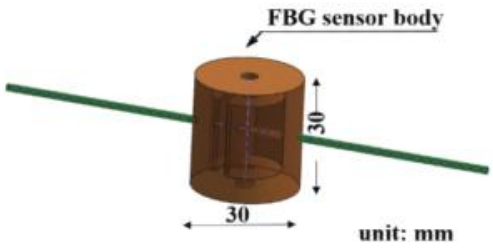

Fig. 6.2 - Diagram of the sensor structure [58].

Three different configurations were proposed as vibration sensors by Bojan Igrec *et al*. [59]. All the configurations proposed are easy to fabricate using a 3D printer and were tested for vibration, showing a linear response and a good bandwidth (>150 Hz). The proposed configurations are lightweight, inexpensive, easy to assemble and repair. The sensor configuration is shown in Fig. 6.3.

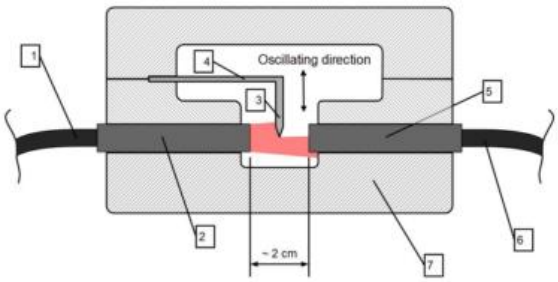

Fig. 6.3 - Diagram of the sensor structure [59].

6.2 Design and embedding the sensor

Three similar sensors were fabricated following the steps proposed in Chapter 4, depicted in Fig. 4.1. The sensors were embedded using a 3D printer with similar structures. The printer was used with a resolution of 250 µm, but is capable of a maximum resolution of 100 µm. The maximum resolution of *x* and *y* position was 50 µm. A schematic version of the used printer is presented in Fig. 6.4.

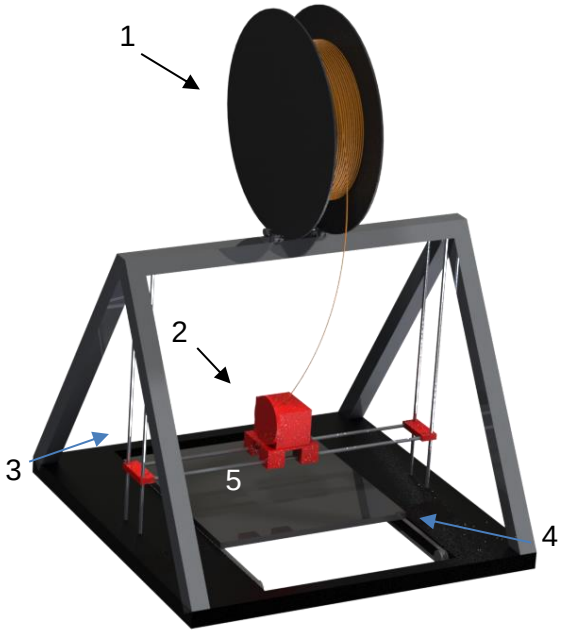

Fig. 6.4 - Scheme of the 3D printer used with: (1) The PLA filament; (2) Position of the extruder and the y positioning motor; (3) Z motor; (4) X motor; (5) Print bed.

A polylactic acid (PLA), a biodegradable thermoplastic, was used in the embedding process. This thermoplastic is one of the most commonly used in desktop 3D printing materials. PLA is an eco-friendly material since it requires less energy to be produced when compared to petroleum-based plastics and it is made from renewable resources. This filament is non-toxic, is available in a wide range of colours and is an easy material to work with, due to its thermal characteristics.

The PLA filament used in the printing process had a 3mm diameter and was extruded at a temperature between 200 and 205°C, using an extruder of 0.4mm diameter. The print bed was kept at 60°C, after the application of a thin layer of spray, to promote the adhesion of the PLA.

The external structure used is composed by two different parts, with the same characteristics. After printing the first part, the sensor is placed in the slit printed with the same dimension and glued using a strong fast-acting adhesive. This glue is placed on the plastic coating of the fiber to not change the characteristics of the sensor. Then, the second part is printed on top of the first part. The complete exostructure with the sensor embedded is presented in Fig. 6.5.

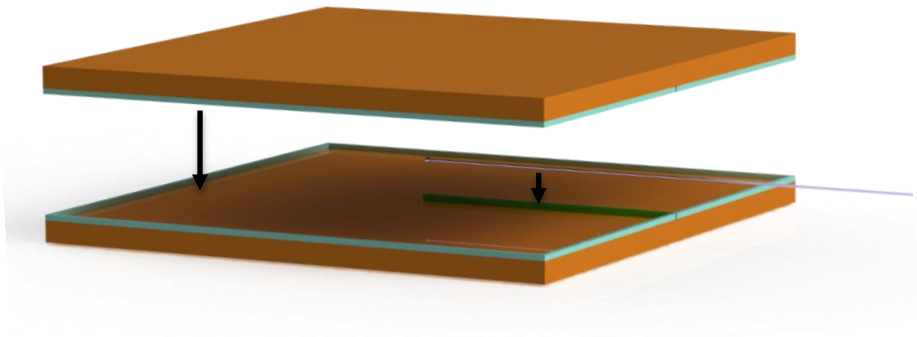

Fig. 6.5 - Exploded view of the embedding 3D printed structure. The internal and external perimeters are shown in green and blue respectively.

The velocity of the process was kept equal in all three exostructures. The first layer was printed with a velocity of 30 mm/s. This layer needs a lower extruding velocity to ease the adhesion of the material to the printing bed. The following layers were printed with a velocity of 40 mm/s, for the external perimeters, and 60 mm/s for internal perimeters and filling.

6.3 Experimental Results

Three sensors were embedded with the structure presented in Fig. 6.7, and tested in lateral loading and temperature. Three sensors with different heights were tested to study the influence of this parameter on the sensor response. In Fig. 6.7, the sensors microscope images are shown. The experimental setup was composed by an optical broadband source (OBS), an optical spectrum analyser (OSA) and an optical circulator connecting all the components to the optical sensor. The OBS used in this work had a bandwidth of 100 nm, centered at 1550 nm. The spectrum was attained in reflection, with the circulator serving as the interrogation system. The experimental setup scheme is presented in Fig. 6.6.

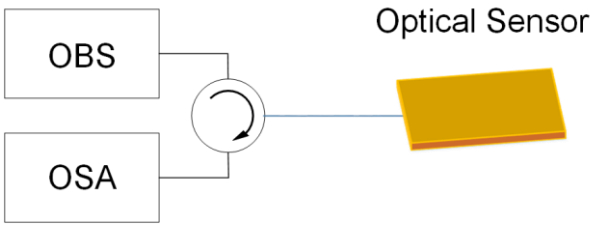

Fig. 6.6 - Experimental setup.

The spectrum of the sensors remained almost unaltered after the embedding process. In Fig. 6.7, the reflection spectra before and after the encasing are presented. An optical power loss is visible in the spectra, while maintaining the original fringes, for all the sensing heads. The power losses due to the embedding of the sensor are summarized in the following table, where the height of the imprinted structure is also given.

Table 6.1 – Optical power loss of the embedded sensors

Denomination	Height of the Structure (mm)	Power Loss (dB)
Sensor 1	1	3.89
Sensor 2	2	3.60
Sensor 3	3	3.70

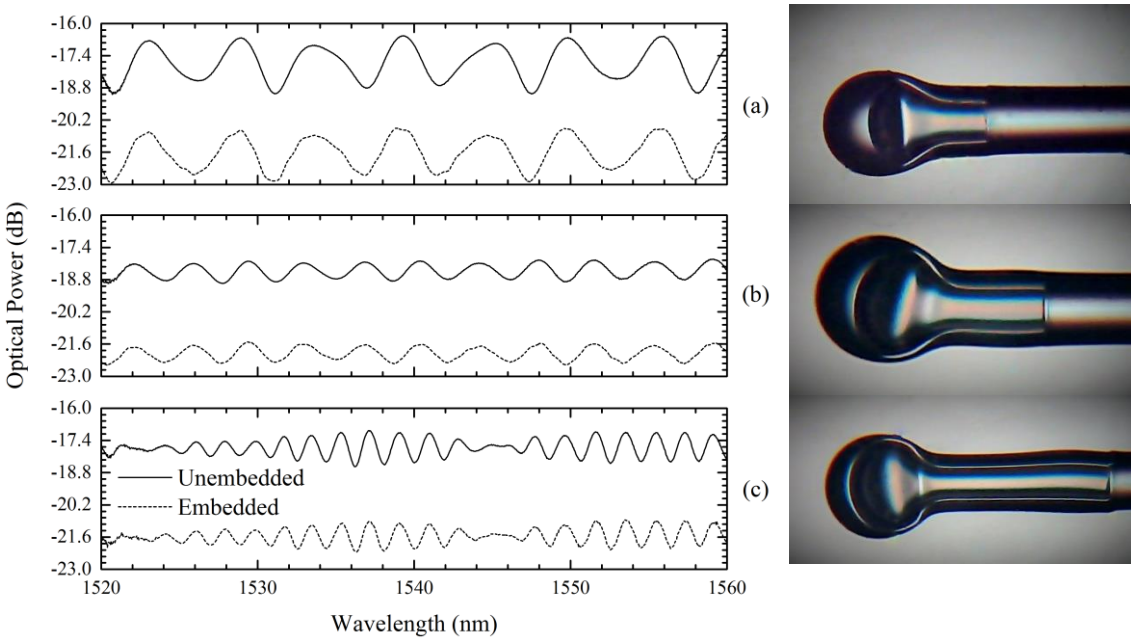

Fig. 6.7 - Reflection spectra of the sensors (a) 1, (b) 2 and (c) 3, before and after being embedded. In the right, the microscope photographs of the sensors are presented.

6.3.1 Lateral Loading Characterization

The lateral loading response was carried out placing the sensor in a press, that applied the pressure evenly throughout the structure. The reflected signal was obtained using the same experimental setup previously presented in Fig. 6.6. The pressure application resulted in an optical power variation in the reflected sensors.

6.3.1.1 Sensor 1

The sensor 1 was tested for lateral loading in pressures ranging from 0 to 157 kPa. Two cycles of pressure were performed, resulting in a linear response of the optical power for pressures between 20 and 133 kPa. The sensor response is shown in Fig. 6.8. The first cycle of loading resulted in a sensitivity of 0.0048±0.0001 dB/kPa, while the second resulted in a lower sensitivity, 0.0024±0.0002 dB/kPa. This sensitivity drop may result on material accommodation due to the pressure applied.

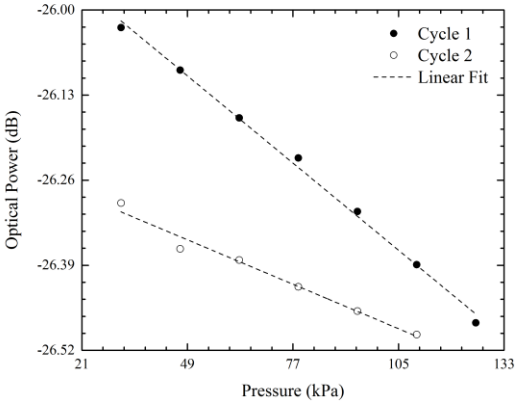

Fig. 6.8 - Pressure response of sensor 1.

6.3.1.2 Sensor 2

The sensor 2 was tested for pressures in the range of 0 to 164 kPa. Two cycles of decreasing pressure were done, attaining a nonlinear response in the range of 40 and 164 kPa, presented in Fig. 6.9. A nonlinear response was obtained, nevertheless the sensor response was similar for both loading cycles. The polynomial fit achieved a r^2 = 0.99 for both loading cycles. The optical power for an applied pressure (kPa) is, for the two cycles, given by:

$$\text{Optical Power (dB)} = -18.33 - 0.01\text{P} + 6.26 \times 10^{-5}\text{P}^2 - 1.02 \times 10^{-5}\text{P}^3 + 3.61 \times 10^{-9}P^4 \quad (6.1)$$

$$\text{Optical Power (dB)} = -18.49 - 3.70 \times 10^{-4}\text{P} + 9.49 \times 10^{-5}\text{P}^2 - 1.83 \times 10^{-6}\text{P}^3 + 7.12 \times 10^{-9}P^4 \quad (6.2)$$

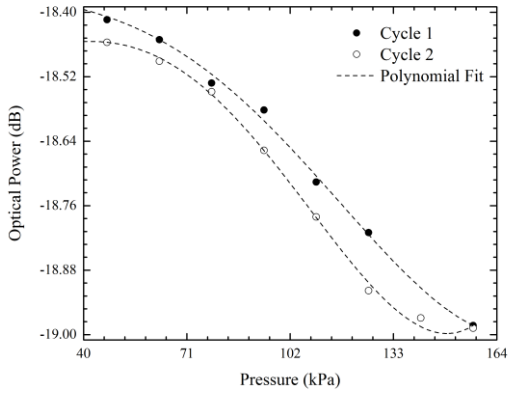

Fig. 6.9 - Sensor 2 response for pressure.

6.3.1.3 Sensor 3

The sensor 3, tested for pressures between 0 and 157 kPa, presented a linear response in all tested range. The sensor, whose response is shown in Fig. 6.10, presented a sensitivity of 0.0037±0.0002 dB/kPa.

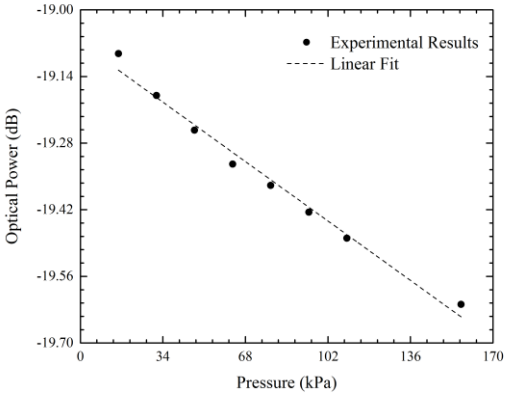

Fig. 6.10 - Pressure response of sensor 3.

6.3.2 Temperature Characterization

6.3.2.1 Sensor 1

Temperature testing was carried out for temperatures ranging from 35 °C and 70 °C. The sensor 1 presented an insensitivity to temperature optical power. The sensors' response is presented in Fig. 6.11.

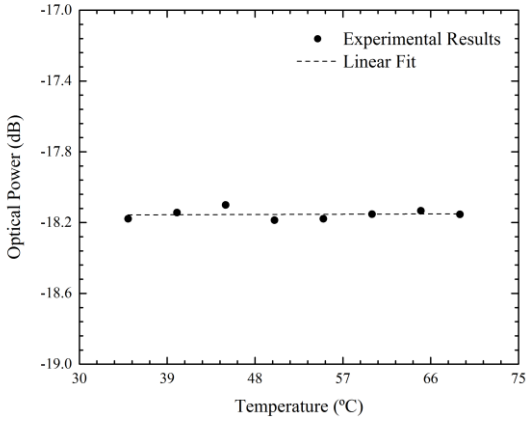

Fig. 6.11 - Temperature response for sensor 1.

6.3.2.2 Sensor 2

The thermal variation applied to sensor 2 resulted in an optical power variation in the reflected spectrum. The response, in Fig. 6.12, was nonlinear with a polynomial fit given by the following expression, for a given temperature *T*(°C):

$$\text{Optical Power (dB)} = -18.82 + 0.01\,\text{T} - 1.3 \times 10^{-4}\text{T}^2 \quad (6.3)$$

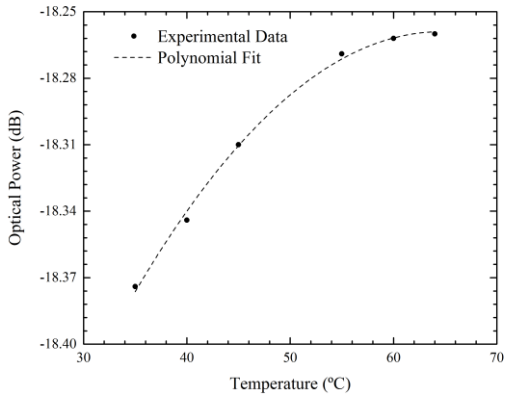

Fig. 6.12 - Optical power response of sensor 2, for temperature variations.

6.3.2.3 Sensor 3

Temperature response was studied in sensor 3 by varying the temperature between 38 °C and 64.5 °C. Thermal variation produced a nonlinear variation in the wavelength, while maintaining the optical power. In Fig. 6.13, the wavelength shift with the applied temperature (°C) is presented. The wavelength shift goes accordingly to the following expression:

$$\text{Wavelength Shift (nm)} = -0.04 - 1.96 \times 10^{-4}\text{T} + 2.97 \times 10^{-5}\text{T}^2 \quad (6.4)$$

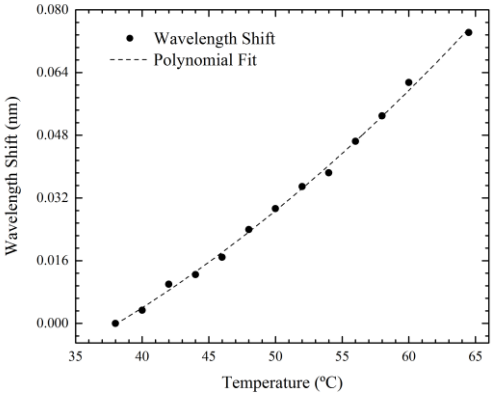

Fig. 6.13 - Wavelength shift with the applied temperature, for sensor 3.

6.3.3 Resolution

The resolution of the sensors was determined by centering the spectrum in a local maximum while acquiring its optical power, for different applied pressures. By choosing the two successive applied pressures with lower optical power difference, the resolution can be calculated. In Fig. 6.14, the points for the two different applied pressures of the three sensors are shown. The achieved resolutions are summarized in Table 6.2.

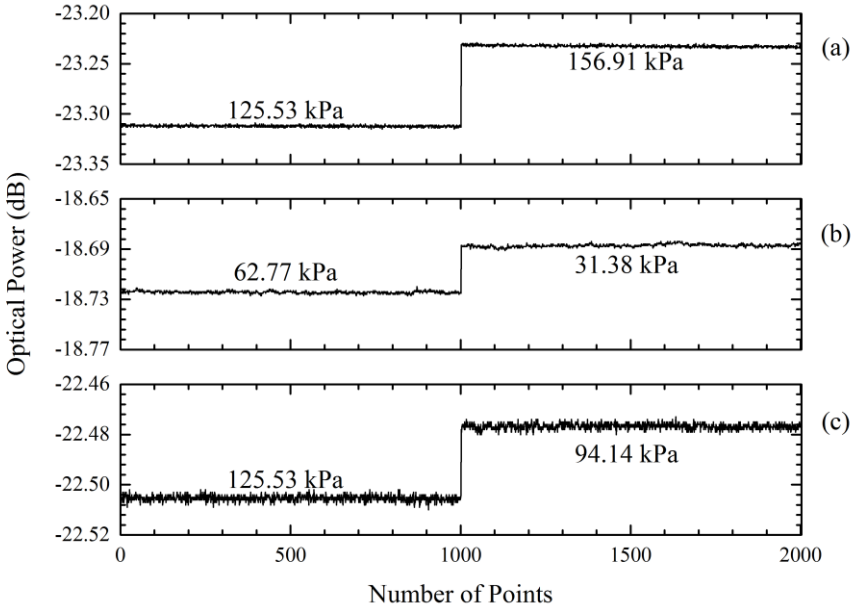

Fig. 6.14 - Variation of maximum optical power for (a) sensor 1, (b) sensor 2 and (c) sensor 3, for two different applied pressures.

Table 6.2 – Resolution of the embedded sensors

Height of the Structure (mm)	Resolution (kPa)
1	**2.75**
2	5.90
3	8.79

6.4 Conclusions

Three optical sensors based on Fabry-Perot interferometry were embedded using a 3D printer. The sensors were characterized in lateral loading and temperature, and the resolution was determined. The sensors embedded in the structure with 1 and 3 mm showed a linear response to lateral loading, while the remaining sensor presented a nonlinear response. Sensor 1, embedded in the 1mm height structure, presented a sensitivity of 0.0048±0.0001 dB/kPa and 0.0024±0.0002 dB/kPa in two subsequent loading cycles for pressures comprised between 20 and 133 kPa. Sensor 2 presented a nonlinear response in the pressure range of 40 to 164 kPa, showing a saturation in the response for pressures below 40 kPa. Two loading cycles were performed in the said sensor and similar behaviour was obtained in both cycles. Sensor 3 presented a linear response for pressures between 0 and 157 kPa, with a sensitivity of 0.0037±0.0002 dB/kPa.

In temperature characterization were attained different behaviours for the studied sensors. Sensor 1 presented an insensitivity for temperature for both wavelength and optical power, while sensor 2 presented a nonlinear response to temperature in optical power while maintaining the fringes original position throughout the temperature characterization. The most promising result was obtained from sensor 3, were only wavelength changes were achieved. The different behaviours can be due to the different ways the sensor is positioned in the exostructure. The resolution of the sensors was estimated and a maximum resolution of 2.75 kPa, was achieved for sensor 1.

The embedding of the sensor brought new application possibilities since the dynamic operation region was highly increased. The proposed sensor can be easily adapted for high pressure measurement, suitable for implementation in harsh environments.

Chapter 7

Concluding Remarks and Future Work

The work developed in the context of this dissertation had the aim of developing new fiber sensor designs with special interest in lateral loading applications. All the sensors developed were based on low finesse Fabry-Perot interferometry and had simple fabrication processes based on the fusion splicing technique. An overview of the technology and applications for sensors based on Fabry-Perot interferometry was fundamental to proceed with the work. The state-of-the-art of this type of sensors was presented in Chapter 2, where a brief introduction on Fabry-Perot interferometry principles was given.

In the chapter 3, a simple curvature sensor fabricated with a hollow core silica fiber was proposed. The simple structure allowed the measurement of low curvatures, with high precision. The sensor design displays a low thermal sensitivity, allowing the application of the sensor in harsh environments.

Over the following chapters, microcavities based on air bubbles were proposed. All the sensors were fabricated using only fusion splicing. The thin silica walls created by this technique translates into a high lateral loading sensitivity. Once again, low thermal sensitivity was attained. A cavity composed by two spheroidal microbubbles was, also, proposed. The sensor design presented very high sensitivity to strain, while presenting a low curvature response. Low thermal sensitivity was, again, attained.

Embedded sensors were proposed over the Chapter 6. The sensors proposed were based on a fiber tip microsphere sensor, embedded in a 3D printer. The printer was able to embed the sensors with high resolution, increasing the dynamic range of operation. Three sensors were embedded with similar encasing structures. These structures, varying only in height, were used for testing lateral loading and temperature. The results, though promising, showed that the encasing structure still needs further improvement. The proposed sensors could be used for high pressure detection, considering that the structure is quite resistant. In the case of the sensor embedded in the structure of 3 mm, thermal variations only give rise to a wavelength shift. This allows the simultaneous monitoring of both measurands.

The work developed in this dissertation can be improved and further investigated. For future work is proposed the following:

- Improving the geometry of the microspheres in order to optimize the sensor sensitivity to lateral loading, in the case of the microsphere sensor tip.
- In the two microsphere sensors, the need to find the optimum geometry to improve the sensors' response is needed.
- Fabrication of the microsphere sensors, in both configurations, with different capillary tube is other interesting matter of study. Different diameters of the hollow fiber could reach to different results, improving the sensitivity of the sensors.
- In the case of the embedded sensors in the 3D printed structures, different encasing geometry can be explored. In particular, different heights for the exostructure or smaller surface of contact with the exterior. Different geometries for the outer structure is other parameter that could potential reach better behaviours for lateral loading applications, enhancing the sensor sensitivity.

Appendix I

Microsphere based sensor for lateral loading measurements

Before using a 3D printed structure to provide embedding for the sensors, a polymer hemisphere was applied. This test was carried out in order to determine if the sensor remained sensible to lateral loading while keeping temperature insensitivity.

Lateral loading was applied to two sensors, embedded in a hemisphere of thermoplastic glue. Four other hemispheres were placed in the same base, forming a square around the sensor. The structure used for lateral loading testes is shown in Fig. 7.1.

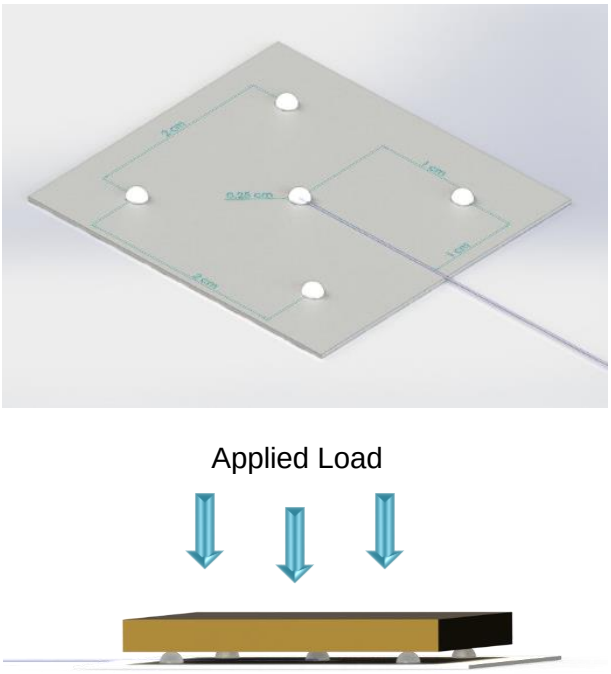

Fig. 7.1 - Structure used for lateral loading measurements. The sensor is placed on the hemisphere in the center of the square.

The experimental setup is composed by a broadband optical source, with a bandwidth of 100 nm centered at 1550 nm, an optical circulator and an optical spectrum analyzer (OSA). The interrogation of the sensing head is provided by the optical circulator, allowing the reflection signal to be read by the OSA, with a resolution of 0.2nm.

The applied load, evenly spread by the five points of application, gives rise to a wavelength shift. One loading and unloading cycle was studied and is shown in the inset of Fig. 7.2. The response is nonlinear and hysteresis is present, due to the polymer characteristics. Considering the loading cycle, the range was divided in two where the behaviour can be approximated to a linear response. A sensitivity of 18 ± 1 pm/N as achieved in the range of 0 to 10 N and a 6.8 ± 0.6 pm/N sensitivity was attained for loads between 10 and 29.5 N.

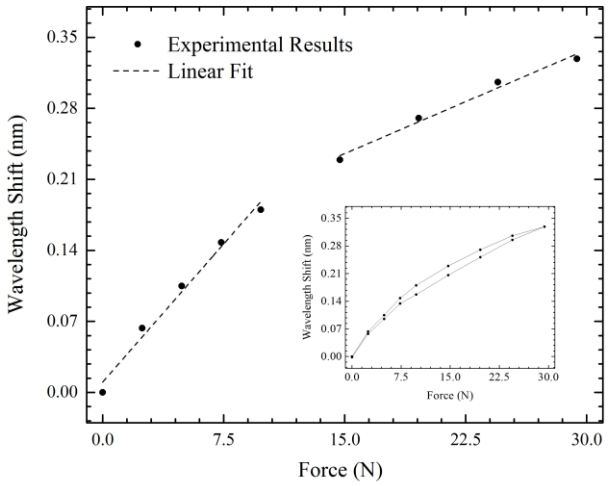

Fig. 7.2 - Wavelength shift response when applying load. Inset: loading and unloading cycle.

The temperature response was also studied for the embedded sensor. The sensor was placed in an oven and the temperature was varied between 40 and 65 ºC. The variation of temperature generates a wavelength shift, shown in Fig. 7.3. The temperature was varied between 45 and 65 ºC, measured with a resolution of 0.1 ºC. A sensitivity of 2.50 ± 0.07pm/ºC was achieved.

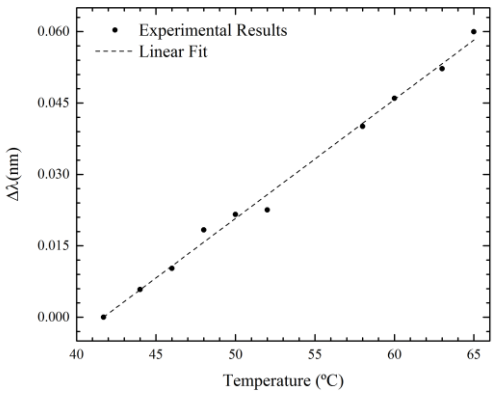

Fig. 7.3 - Temperature response of the sensor, in wavelength.

Conclusions

By using the fabrication principles presented in Chapter 4, a sensor was fabricated and embedded in a hemisphere of a thermoplastic. This material, a polymer, was able to enlarge the range of operation of the sensor. That is, the sensor can resist to larger applied loads without breaking. The embedding of the sensor on a polymer generates a hysteresis due to the material mechanical response and a sensibility drop. The sensor presented a high temperature response, with a maximum cross-sensitivity of 0.4 N/ºC, however showed a linear behaviour on the studied range.

The results obtained allowed the development of a sensor embedded on a 3D printed structure, presented in Chapter 6.

Appendix II

3D printed designs for lateral loading sensors

In order to reach the results presented in Chapter 6, multiple embedding designs were tested. The first printed embed design was similar to the polymer embedding tested. The hemispheres used in the polymer encasing were replaced by cubes with similar dimensions. This modification on the design was due to difficulties in printing small circular structures. The design used is presented in Fig. 7.4.

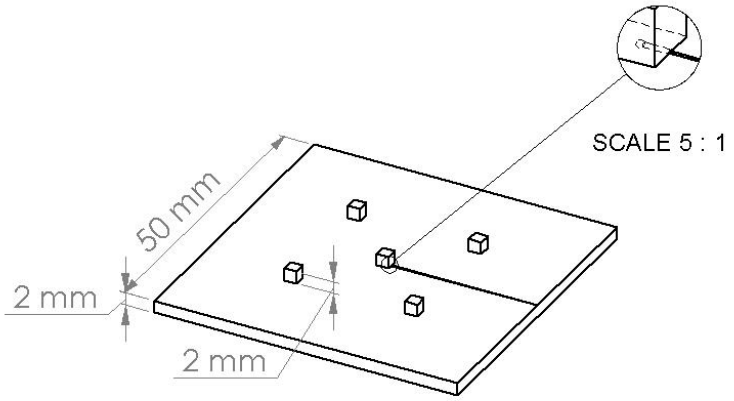

Fig. 7.4 - Exostructure tested with a similar structure as the polymer embedded sensor.

Other tested geometry is presented in Fig. 7.5. The design was similar to the previous imprinted structure, but the imbalance of the applied load is different.

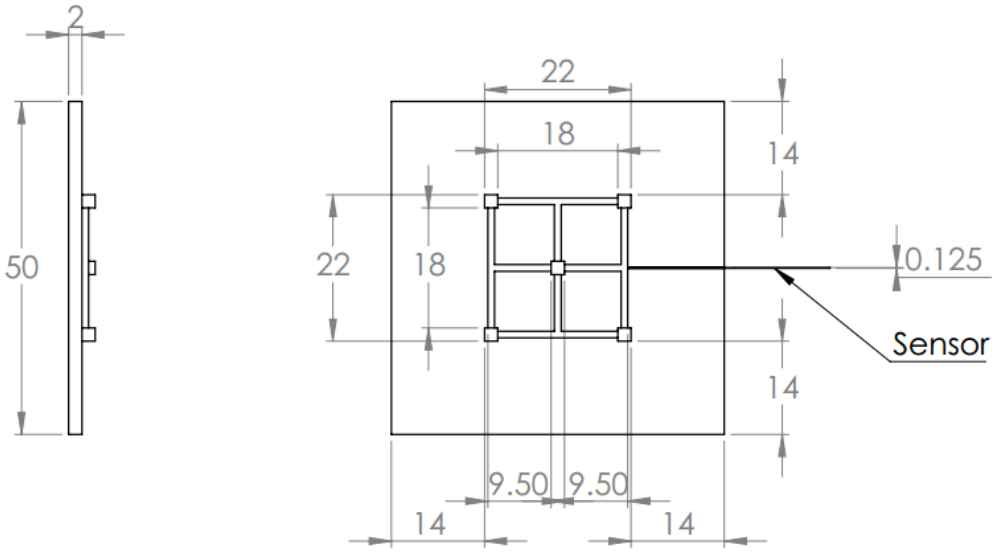

Fig. 7.5 - Lateral and top view of other proposed 3D printed structure. The measures are presented in mm.

For further testing, the geometry of the structure was changed to a flat surface, with smaller surface area, as presented in Chapter 6. The material used in the structure was a PLA, with the following specifications:

Table 7.1 – Specifications of the extruded material

Filament Diameter	3 mm
Printing Temperature	190 – 220 ºC
Printing Bed Temperature	60 – 80 ºC
Impact Strength	5 KJ/m^2
Density	1.25 g/cm^3 (at 21.5ºC)
Glass Transition Temperature	~50ºC

References

[1] D. a. Jackson and J. D. C. Jones, “Fibre Optic Sensors,” *Opt. Acta Int. J. Opt.*, vol. 33, no. 12, pp. 1469–1503, Dec. 1986.

[2] B. H. Lee, Y. H. Kim, K. S. Park, J. B. Eom, M. J. Kim, B. S. Rho, and H. Y. Choi, “Interferometric fiber optic sensors,” *Sensors*, vol. 12, no. 3, pp. 2467–2486, 2012.

[3] P. Roriz, O. Frazão, A. B. Lobo-Ribeiro, J. L. Santos, and J. A. Simões, “Review of fiber-optic pressure sensors for biomedical and biomechanical applications,” *J. Biomed. Opt.*, vol. 18, no. 5, p. 50903, 2013.

[4] G. B. Hocker, “Fiber-optic sensing of pressure and temperature.,” *Appl. Opt.*, vol. 18, no. 9, pp. 1445–1448, 1979.

[5] A. Dandridge and A. B. Tveten, “Phase compensation in interferometric fiber-optic sensors.,” *Opt. Lett.*, vol. 7, no. 6, pp. 279–281, 1982.

[6] M. Imai, T. Ohashi, and Y. Ohtsuka, “High-sensitive all-fiber Michelson interferometer by use of differential output configuration,” *Opt. Commun.*, vol. 39, no. 1, pp. 7–10, 1981.

[7] E. Udd, “Fiber-Optic Acoustic Sensor Based on the Sagnac Interferometer,” *Proc. Soc. Photo-Optical Instrum. Eng.*, vol. 425, pp. 90–95, 1983.

[8] J. S. Sirkis, D. D. Brennan, M. A. Putman, T. A. Berkoff, A. D. Kersey, and E. J. Friebele, “In-Line Fiber Etalon for Strain-Measurement,” *Opt. Lett.*, vol. 18, no. 22, pp. 1973–1975, 1993.

[9] M. S. Ferreira, P. Roriz, J. Bierlich, J. Kobelke, K. Wondraczek, C. Aichele, K. Schuster, J. L. Santos, and O. Frazão, “Fabry-Perot cavity based on silica tube for strain sensing at high temperatures,” *Opt. Express*, vol. 23, no. 12, p. 16063, 2015.

[10] J. Sirkis, T. A. Berkoff, R. T. Jones, H. Singh, A. D. Kersey, E. J. Friebele, and M. A. Putnam, “In-line fiber etalon (ILFE) fiber-optic strain sensors,” *J. Light. Technol.*, vol. 13, no. 7, pp. 1256–1263, 1995.

[11] M. S. Ferreira, P. Roriz, S. O. Silva, J. L. Santos, and O. Frazão, “Next

generation of Fabry-Perot sensors for high-temperature," *Opt. Fiber Technol.*, vol. 19, no. 6 PART B, pp. 833–837, 2013.

[12] E. Cibula, D. Donlagic, and C. Stropnik, "Miniature fiber optic pressure sensor for medical applications," *Sensors. Proc. IEEE*, vol. 1, pp. 711–714, 2002.

[13] D. Donlagic and E. Cibula, "All-fiber high-sensitivity pressure sensor with SiO2 diaphragm.," *Opt. Lett.*, vol. 30, no. 16, pp. 2071–2073, 2005.

[14] Y. Zhu and A. Wang, "Miniature fiber-optic pressure sensor," *IEEE Photonics Technol. Lett.*, vol. 17, no. 2, pp. 447–449, 2005.

[15] K. D. Oh, J. Ranade, V. Arya, A. Wang, and R. O. Claus, "Optical Fiber Fabry – Perot Interferometric Sensor for Magnetic Field Measurement," *IEEE Photonics Technol. Lett.*, vol. 9, no. 6, pp. 797–799, 1997.

[16] R. Q. Lv, Y. Zhao, D. Wang, and Q. Wang, "Magnetic fluid-filled optical fiber Fabry-P??rot sensor for magnetic field measurement," *IEEE Photonics Technol. Lett.*, vol. 26, no. 3, pp. 217–219, 2014.

[17] T. Yoshino, K. Kurosawa, K. Itoh, and T. Ose, "Fiber-Optic Fabry-Perot Interferometer and its Sensor Applications," *IEEE Trans. Microw. Theory Tech.*, vol. 30, no. 10, pp. 1612–1621, 1982.

[18] J. P. Dakin, C. A. Wade, and P. B. Withers, "An optical fibre sensor for the measurement of pressure," *Fiber Integr. Opt.*, vol. 7, no. 1, pp. 35–46, 1988.

[19] T. Liu and G. F. Fernando, "A frequency division multiplexed low-finesse fiber optic Fabry–Perot sensor system for strain and displacement measurements," *Rev. Sci. Instrum.*, vol. 71, no. 3, p. 1275, 2000.

[20] T. Katsumata, Y. Haga, K. Minami, and M. Esashi, "Micromachined 125 μm diameter ultra miniature fiber-optic pressure sensor for catheter," *Trans. Inst. Electr. Eng. Japan*, vol. 120, no. 2, pp. 58–63, 2000.

[21] J. Xu, X. Wang, K. L. Cooper, and A. Wang, "Miniature all-silica fiber optic pressure and acoustic sensors.," *Opt. Lett.*, vol. 30, no. 24, pp. 3269–3271, 2005.

[22] S. Watson, M. J. Gander, W. N. MacPherson, J. S. Barton, J. D. C. Jones, T. Klotzbuecher, T. Braune, J. Ott, and F. Schmitz, "Laser-machined fibers as

Fabry-Perot pressure sensors.," *Appl. Opt.*, vol. 45, no. 22, pp. 5590–6, 2006.

[23] X. Wang, J. Xu, Y. Zhu, K. L. Cooper, and A. Wang, "All-fused-silica miniature optical fiber tip pressure sensor," *Opt. Lett.*, vol. 31, no. 7, pp. 885–7, 2006.

[24] Y. J. Rao, "In-line fiber-optic etalon formed by hollow-core photonic crystal fiber," *2007 Asia Opt. Fiber Commun. Optoelectron. Expo. Conf. AOE*, vol. 1, pp. 124–126, 2007.

[25] M. Deng, C.-P. Tang, T. Zhu, Y.-J. Rao, L.-C. Xu, and M. Han, "Refractive index measurement using photonic crystal fiber-based Fabry-Perot interferometer.," *Appl. Opt.*, vol. 49, no. 9, pp. 1593–1598, 2010.

[26] M. S. Ferreira, L. Coelho, K. Schuster, J. Kobelke, J. L. Santos, and O. Frazão, "Fabry-Perot cavity based on a diaphragm-free hollow-core silica tube.," *Opt. Lett.*, vol. 36, no. 20, pp. 4029–31, 2011.

[27] J. Ma, J. Ju, L. Jin, W. Jin, and D. Wang, "Fiber-tip micro-cavity for temperature and transverse load sensing.," *Opt. Express*, vol. 19, no. 13, pp. 12418–12426, 2011.

[28] D. H. Wang, S. J. Wang, and P. G. Jia, "In-line silica capillary tube all-silica fiber-optic Fabry-Perot interferometric sensor for detecting high intensity focused ultrasound fields.," *Opt. Lett.*, vol. 37, no. 11, pp. 2046–8, 2012.

[29] D.-W. Duan, Y.-J. Rao, Y.-S. Hou, and T. Zhu, "Microbubble based fiber-optic Fabry-Perot interferometer formed by fusion splicing single-mode fibers for strain measurement.," *Appl. Opt.*, vol. 51, no. 8, pp. 1033–6, 2012.

[30] R. Wang and X. Qiao, "Gas refractometer based on optical fiber extrinsic fabry - Perot interferometer with open cavity," *IEEE Photonics Technol. Lett.*, vol. 27, no. 3, pp. 245–248, 2015.

[31] C.-L. Lee, H.-Y. Ho, J.-H. Gu, T.-Y. Yeh, and C.-H. Tseng, "Dual hollow core fiber-based Fabry-Perot interferometer for measuring the thermo-optic coefficients of liquids," *Opt. Lett.*, vol. 40, no. 4, pp. 459–462, 2015.

[32] Q. Rong, H. Sun, X. Qiao, J. Zhang, M. Hu, and Z. Feng, "A miniature fiber-optic temperature sensor based on a Fabry – Perot interferometer," *J. Opt.*, vol. 45002, no. 14, 2012.

[33] Q. Zhang, T. Zhu, Y. Hou, and K. S. Chiang, “All-fiber vibration sensor based on a Fabry–Perot interferometer and a microstructure beam,” *J. Opt. Soc. Am. B*, vol. 30, no. 5, pp. 1211–1215, 2013.

[34] G. Z. Xiao, A. Adnet, Z. Zhang, F. G. Sun, and C. P. Grover, “Monitoring changes in the refractive index of gases by means of a fiber optic Fabry-Perot interferometer sensor,” *Sensors Actuators, A Phys.*, vol. 118, no. 2, pp. 177–182, 2005.

[35] H. Gong, H. Song, X. Li, J. Wang, and X. Dong, “An optical fiber curvature sensor based on photonic crystal fiber modal interferometer,” *Sensors Actuators, A Phys.*, vol. 195, pp. 139–141, 2013.

[36] M. Cano-Contreras, A. D. Guzman-Chavez, R. I. Mata-Chavez, E. Vargas-Rodriguez, D. Jauregui-Vazquez, D. Claudio-Gonzalez, J. M. Estudillo-Ayala, R. Rojas-Laguna, and E. Huerta-Mascotte, “All-Fiber Curvature Sensor Based on an Abrupt Tapered Fiber and a Fabry–Pérot Interferometer,” *IEEE Photonics Technol. Lett.*, vol. 26, no. 22, pp. 2213–2216, 2014.

[37] C. S. Shin and M. W. Lin, “An optical fiber-based curvature sensor for endodontic files inside a tooth root canal,” *IEEE Sens. J.*, vol. 10, no. 6, pp. 1061–1065, 2010.

[38] M. J. Weber, a V Dotsenko, L. B. Glebov, and V. a Tsekhomsky, *Handbook of Optical Materials*, vol. 23, no. 1. 2003.

[39] M. S. Ferreira, K. Schuster, J. Kobelke, J. L. Santos, and O. Frazão, “Spatial optical filter sensor based on hollow-core silica tube.,” *Opt. Lett.*, vol. 37, no. 5, pp. 890–2, 2012.

[40] M. Da Zhou, C. Yang, Z. Liu, J. P. Cysyk, and S. Y. Zheng, “An implantable Fabry-Pérot pressure sensor fabricated on left ventricular assist device for heart failure,” *Biomed. Microdevices*, vol. 14, no. 1, pp. 235–245, 2012.

[41] J. M. Lopez-Higuera, L. Rodriguez Cobo, A. Quintela Incera, and A. Cobo, “Fiber Optic Sensors in Structural Health Monitoring,” *J. Light. Technol.*, vol. 29, no. 4, pp. 587–608, 2011.

[42] M. J. Gander, W. N. MacPherson, J. S. Barton, R. L. Reuben, J. D. C. Jones, R. Stevens, K. S. Ghana, S. J. Andersen, and T. V. Jones, “Embedded

micromachined fiber-optic fabry-perot pressure sensors in aerodynamics applications," *IEEE Sens. J.*, vol. 3, no. 1, pp. 102–107, 2003.

[43] C. Liao, S. Liu, L. Xu, C. Wang, Y. Wang, Z. Li, Q. Wang, and D. N. Wang, "Sub-micron silica diaphragm-based fiber-tip Fabry–Perot interferometer for pressure measurement," *Opt. Lett.*, vol. 39, no. 10, p. 2827, 2014.

[44] Y. Zhu, K. L. Cooper, G. R. Pickrell, and A. Wang, "High-temperature fiber-tip pressure sensor," *J. Light. Technol.*, vol. 24, no. 2, pp. 861–869, 2006.

[45] X. Chen, F. Shen, Z. Wang, Z. Huang, and A. Wang, "Micro-air-gap based intrinsic Fabry-Perot interferometric fiber-optic sensor," *Appl. Opt.*, vol. 45, no. 30, pp. 7760–7766, 2006.

[46] C. R. Liao, T. Y. Hu, and D. N. Wang, "Optical fiber Fabry-Perot interferometer cavity fabricated by femtosecond laser micromachining and fusion splicing for refractive index sensing," *Opt. Express*, vol. 20, no. 20, p. 22813, 2012.

[47] D. Jáuregui-Vázquez, J. M. Estudillo-Ayala, R. Rojas-Laguna, E. Vargas-Rodríguez, J. M. Sierra-Hernández, J. C. Hernández-García, and R. I. Mata-Chávez, "An all fiber intrinsic Fabry-Perot interferometer based on an air-microcavity," *Sensors (Switzerland)*, vol. 13, no. 5, pp. 6355–6364, 2013.

[48] S. Liu, Y. P. Wang, C. R. Liao, G. J. Wang, Z. Y. Li, Q. Wang, J. T. Zhou, K. M. Yang, X. Y. Zhong, J. Zhao, and J. Tang, "High-sensitivity strain sensor based on in-fiber improved Fabry-Perot interferometer," *Opt. Lett.*, vol. 39, no. 7, pp. 2121–2124, 2014.

[49] A. Zhou, B. Y. Qin, Z. Zhu, Y. X. Zhang, Z. H. Liu, J. Yang, and L. B. Yuan, "Hybrid structured fiber-optic Fabry-Perot interferometer for simultaneous measurement of strain and temperature," *Opt. Lett.*, vol. 39, no. 18, pp. 5267–5270, 2014.

[50] M. S. Ferreira, J. L. Santos, and O. Frazão, "Silica microspheres array strain sensor.," *Opt. Lett.*, vol. 39, no. 20, pp. 5937–40, 2014.

[51] H. Van De Stadt and J. M. Muller, "Multimirror Fabry-Perot interferometers," *J. Opt. Soc. Am. A*, vol. 2, no. 8, 1985.

[52] P. Walters and K. Davies, "3D printing for artists: Research and creative practice," vol. 96, no. 2002, pp. 1–6, 2010.

[53] C. H. Séquin, “Rapid Prototyping: A 3D Visualization Tool Takes on Sculpture and Mathematical Forms,” *Commun. ACM*, vol. 48, no. 6, pp. 66–73, 2005.

[54] C. Bergmann, M. Lindner, W. Zhang, K. Koczur, A. Kirsten, R. Telle, and H. Fischer, “3D printing of bone substitute implants using calcium phosphate and bioactive glasses,” *J. Eur. Ceram. Soc.*, vol. 30, no. 12, pp. 2563–2567, 2010.

[55] S. J. Leigh, R. J. Bradley, C. P. Purssell, D. R. Billson, and D. A. Hutchins, “A Simple, Low-Cost Conductive Composite Material for 3D Printing of Electronic Sensors,” *PLoS One*, vol. 7, no. 11, pp. 1–6, 2012.

[56] J. T. Muth, D. M. Vogt, R. L. Truby, Y. Mengüç, D. B. Kolesky, R. J. Wood, and J. A. Lewis, “Embedded 3D printing of strain sensors within highly stretchable elastomers,” *Adv. Mater.*, vol. 26, no. 36, pp. 6307–6312, 2014.

[57] M. G. Zubel, K. Sugden, D. Saez-Rodriguez, K. Nielsen, and O. Bang, “3D printed sensing patches with embedded polymer optical fibre Bragg gratings,” vol. 9916, p. 99162E, 2016.

[58] Y. Lin, T. Hsieh, L. Tsai, S. Wang, and C. Chiang, “Using Three-Dimensional Printing Technology to Produce a Novel Optical Fiber Bragg Grating Pressure Sensor,” *Sensors Mater.*, vol. 28, no. 5, pp. 389–394, 2016.

[59] B. Igrec, M. Bosiljevac, Z. Sipus, D. Babic, and S. Rudan, “Fiber-optic vibration sensor for high-power electric machines realized using 3D printing technology,” vol. 9754, p. 975410, 2016.